4 Results

4.1 Purification and 3D-structure analysis of rat CD26/DPPIV

4.1.1 Purification of homogeneous dimeric rat CD26/DPPIV with enzyme activity

Purification procedure was shown in Fig. 2. The rat CD26 was expressed in CHO cells (CHO/CD26 cells) (Fan et al., 1997). Enzymatically active CD26/DPPIV was isolated from mAb 13.4-conjugated affinity chromatography. Homogeneous dimeric DPPIV/CD26 with enzymatic activity was subsequently purified by size-exclusion fast protein liquid chromatography (SE-FPLC).

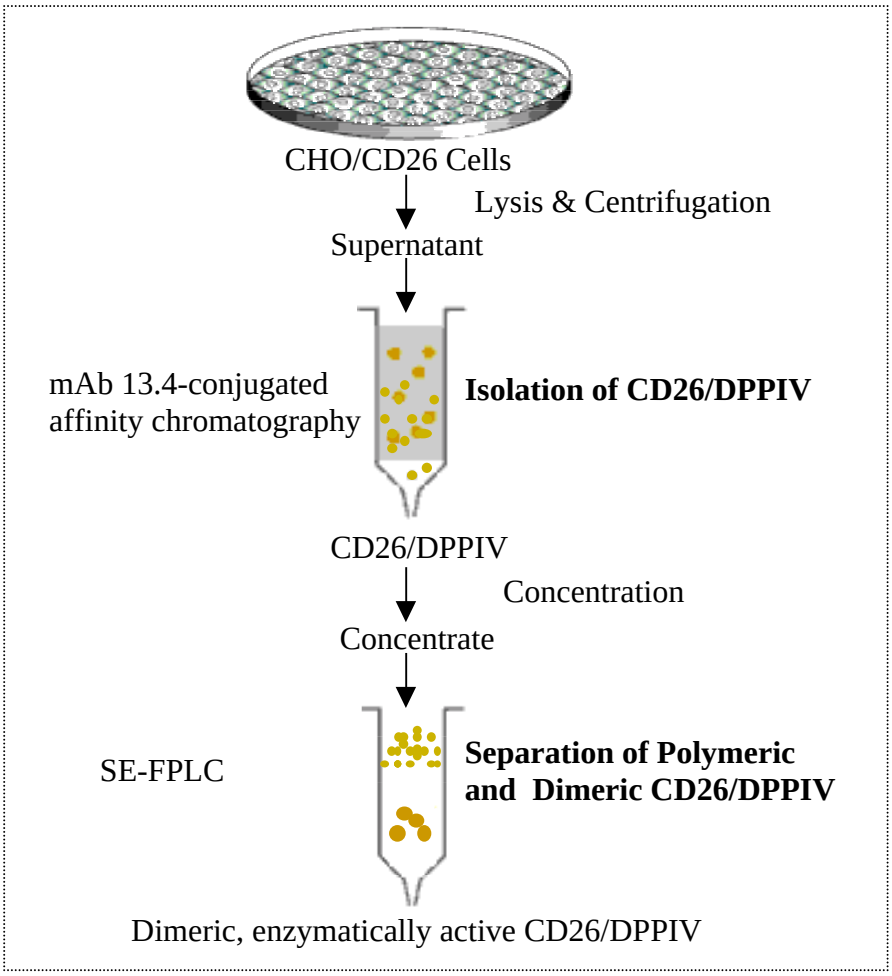

Fig. 2. Schematic diagram of isolation and purification of homogeneous dimeric rat CD26/DPPIV with enzyme activity.

Non-denaturing PAGE followed by silver staining and enzymatic activity assay revealed that highly purified active DPPIV/CD26 was separated from affinity column. Fractions 2-6, showing higher protein concentration as well as enzyme activity (Fig. 3), were pooled and concentrated to 250-300 µl by using an Ultrafree-4 centrifugation unit with a Biomax-30 membrane (UFV4BTK25, Millipore). The molecules below 30 kDa were removed by centrifugation and elution buffer was replaced with PBS for further purification by SE-FPLC.

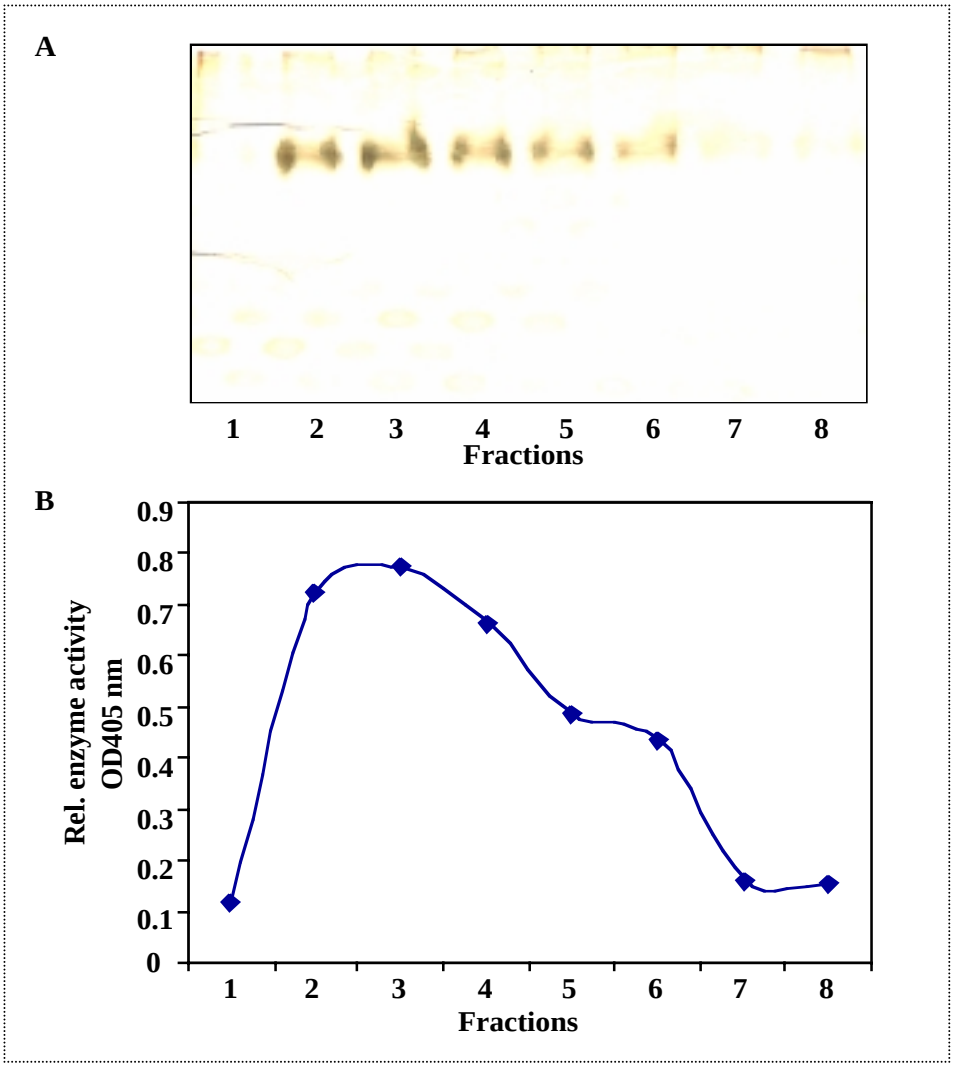

Fig. 3. Isolation of rat CD26 with enzyme activity by mAb 13.4-conjugated affinity column. A. Silver-stained polyacrylamide gel electrophoresis under non-denaturing conditions. **B.** Analysis of enzymatic activity.

An additional SE-FPLC gel filtration step was performed to isolate dimeric DPPIV/CD26. The typical elution profile of rat DPPIV/CD26 from SE-FPLC was shown in Fig. 4B. In comparison with the standard proteins (Fig. 4A), four peaks (1, 2, 3 and 4) corresponded to Mr 3140 k, 650 k, 210 k and 5 k, respectively (Fig. 4B). The proteins in peaks 1, 2 and 3 showed DPPIV enzymatic activity (Fig. 4C), which should correspond to polymer, hexamer and dimer of CD26, respectively. The peak 3, corresponding to dimeric DPPIV/CD26 with Mr of 210 k, appeared at 11-13 ml (Fractions 23-26). Combining enzymatic activity assay with silver staining of non-denaturing PAGE indicated that this purification protocol yielded homogeneous dimeric protein with high enzymatic activity (Fig. 4C and 5A). The eluted fractions with dimeric proteins were analyzed further by SDS-PAGE. As shown in Fig. 5B, although fractions 23 to 26 contained dimeric proteins by non-denaturing gel electrophoresis, fraction 26 obviously gave two different monomeric bands. Fan et al. (Fan et al., 1997) reported that DPPIV/CD26 in CHO transfectants is initially synthesized as a 100 kDa monomer containing only mannose-rich glycans; after processing, mannose-rich glycans are converted into complex oligosaccharides and Mr of monomer increases to 110 kDa. According to this, proteins in fraction 26 consisted of dimeric CD26/DPPIV containing not only mature but also mannose-rich *N*-glycans. Considering that fraction 25 may contain also trace amount of proteins with mannose-rich *N*-glycans, only fraction 24 containing proteins with homogeneous mature *N*-glycan structure of complex form was used for further 3D-structure elucidation by cryo-transmission electron microscopy.

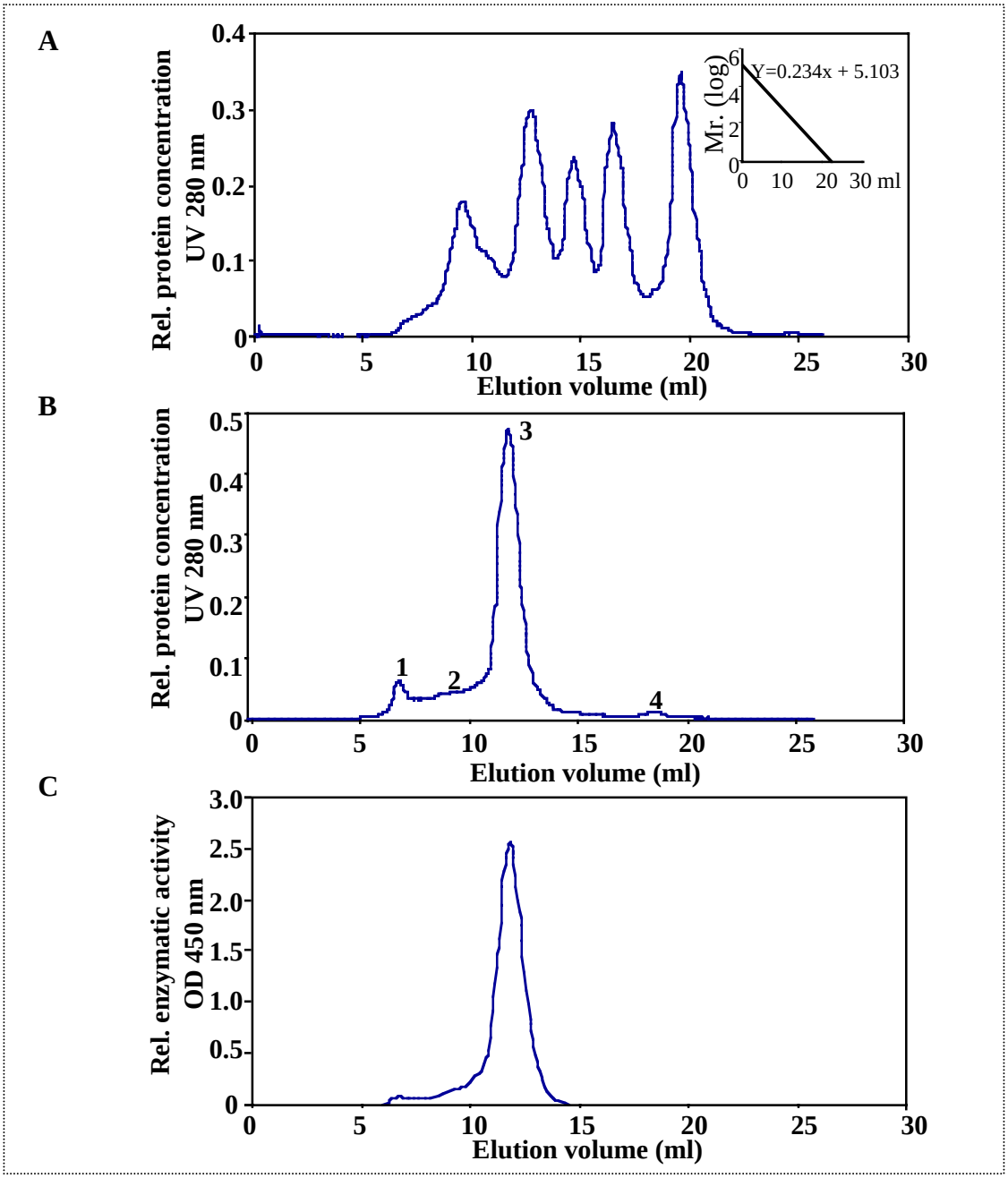

Fig. 4. Isolation of homogeneous dimeric CD26 by size exclusion chromatography. **A.** Elution profile of standard proteins. The standard linear regression curve was generated by plotting the log of the molecular mass of different calibration proteins against their elution volume (see insert). Standard protein is thyroglobulin (670 kDa), aldolase (156 kDa), ovalbumin (44 kDa), cytochrome c (17 kDa), and cobalamin (1.35 kDa), respectively. **B.** Typical elution profile of rat DPPIV/CD26 after size exclusion chromatography on a Superdex 200 column. **C.** Analysis of enzymatic activity.

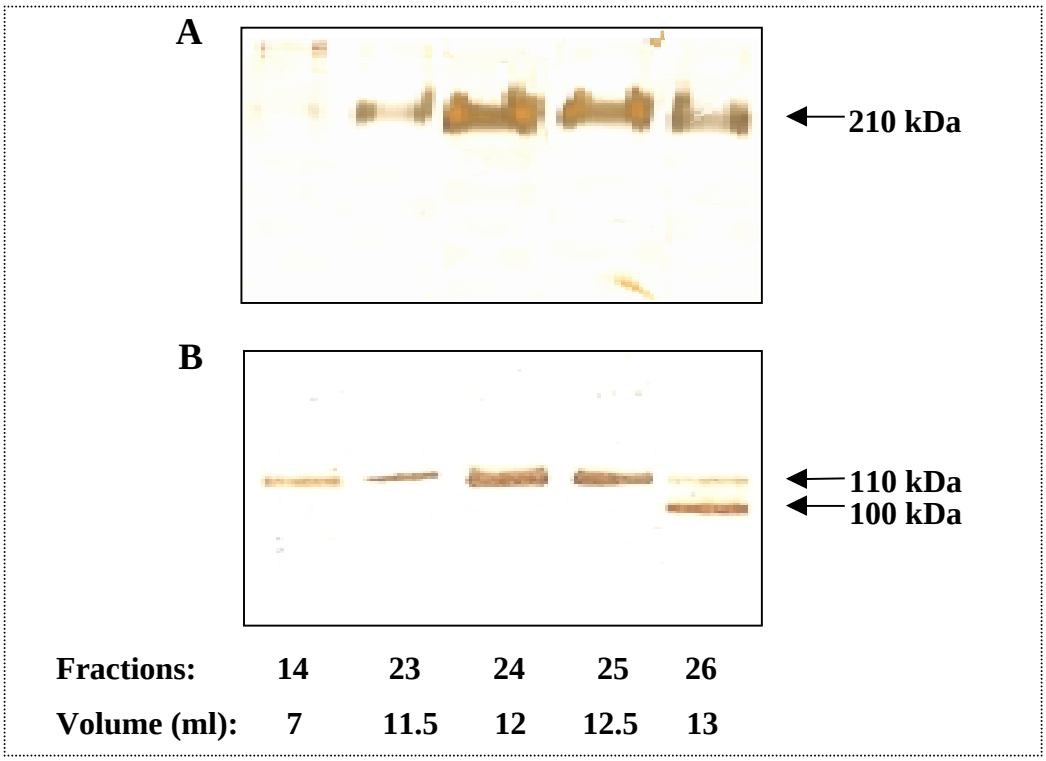

Fig. 5. Purity check of fractions separated by FPLC. A. Silver-stained polyacrylamide gel electrophoresis under non-denaturing conditions. **B.** Silver-stained SDS-PAGE.

4.1.2 The 3D-structure of rat DPPIV/CD26 as obtained by cryo-TEM and single particle analysis

(Cooperation with Dr. Christoph Böttcher and Dr. Kai Ludwig, Forschungszentrum für Elektronenmikroskopie, Freie Universität Berlin)

The three-dimensional structure of this protein was determined at a resolution of ~14 Å applying cryo-electron microscopy and angular reconstitution techniques to single particle preparations. An electron micrograph of CD26 dimer was shown in Fig. 6. 11,121 single molecules were interactively selected and used for the three-dimensional reconstruction. All reconstruction procedures were performed without application of symmetry restraints. The obtained 3D-structure can be described as two distinct, nearly identical barrel-shaped subunits, which are connected by two well-defined bridges, confirming the expected dimeric organization of the protein (Fig. 7).

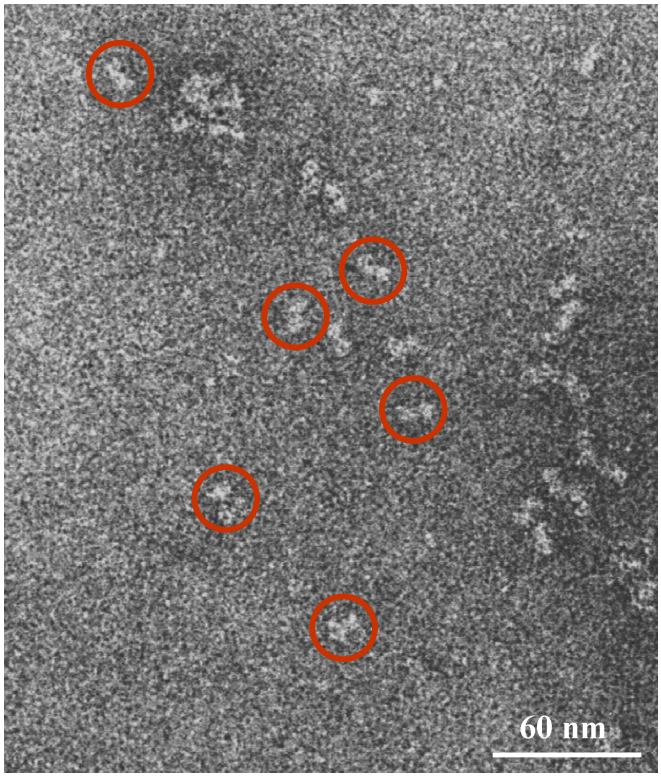

Fig. 6. An electron micrograph of CD26 dimer.

The subunits are tilted against each other at an angle of approximately 120° when the molecule is observed from the side (Fig. 7A). Viewed longitudinally, the subunits are also twisted against each other (Fig. 7B and 7C). The overall length of the dimer is ~120 Å, whereas the individual monomers measure ~70 Å in length and ~65 Å in diameter. The threshold of the depicted surface representation was chosen to correspond to the experimentally determined Mr of 210 kDa. Glycosylated sites in the molecule, which tend to be highly flexible, do not contribute to the density map.

The most prominent features of the reconstruction are two openings observed in each of the two subunits, creating a central channel through each monomer. In its central part each channel widens to form a substantial cavity. One opening (18 Å diam.) is located distally at the outer top face of each monomer, while the second (23 Å diam.) is located in the side just below a massive bulge bending from the top. The overall spatial organization, which is noticeably characterized by the preferential alignment of its two subunits towards one side,

suggests a plausible orientation in the membrane: if one considers the distal openings to be the entrance or exit sites for the uptake or release of substrates, they should be preferentially directed away from the membrane (Fig. 7A and B).

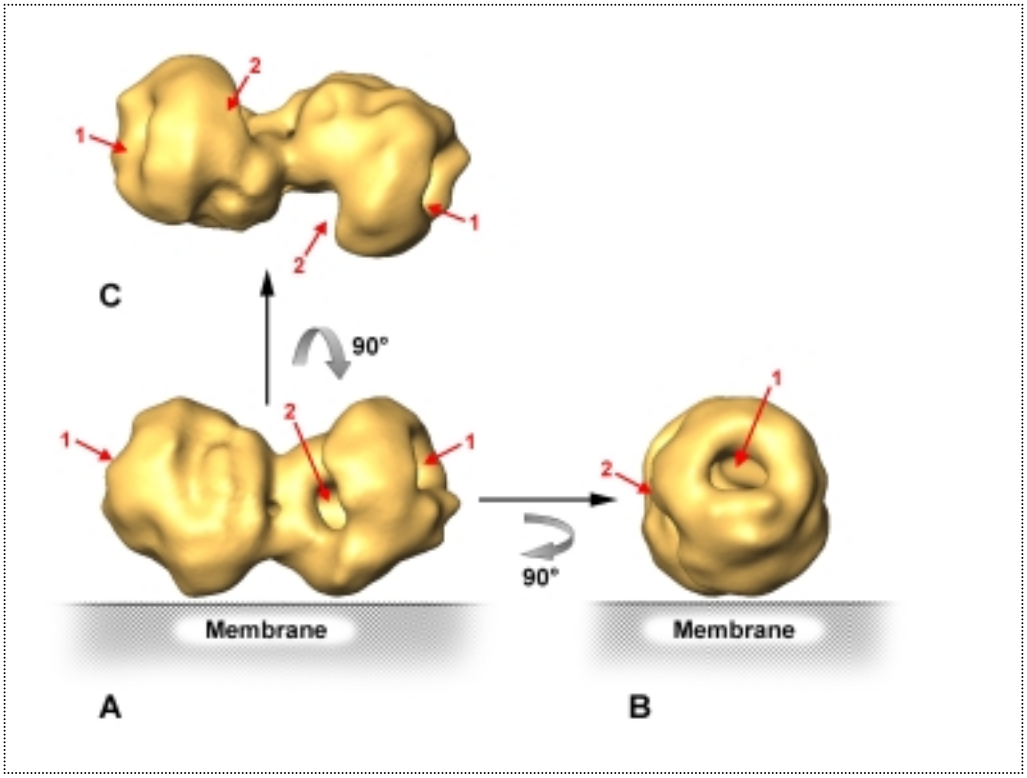

Fig. 7. Surface representations of the 3D-reconstruction of rat DPPIV/CD26 at a resolution of ~14 Å, determined from cryo-electron micrographs and single particle analysis. The distal opening **1.** and the lateral opening **2.** are indicated by red arrows (for further description see text). **A.** Side view. **B.** Side view rotated (in-plane) by 90°. **C.** Top view. The putative localization of the cellular membrane is schematically indicated in **A** and **B**.

There are several indications in the literature of close structural analogies of DPPIV/CD26 and prolyl oligopeptidase (POP, EC 3.4.21.26). These findings are based on sequence alignments, structure simulations/models, CD and FTIR spectroscopy (Durinx et al., 2000) (Lambeir et al., 2001). The endopeptidase POP, which cleaves after proline, is also a serine peptidase; like DPPIV/CD26 it possesses a catalytic site consisting of a Gly-X-Ser-X-Gly

conserved sequence. Based on the known crystal structure of POP and three-dimensional structure predictions (Brandt, 2000) (Gorrell et al., 2001), the following structural elements are expected for DPPIV/CD26:

(a) A β-propeller domain
(b) A compact α/β–hydrolase domain including the catalytic triad Ser, His and Asp (as in POP S554 H680 and D641)
(c) A central cavity, providing space for access of substrates to the catalytic site.

On the basis of these expected structural motifs we performed docking calculations and tried to fit the density map of the known POP crystal structure (pdb-entry: 1qfm) into our EM-structure. At first sight, the result of this calculation reveals certain similarities, such as the overall dimensions and the general spatial organization (Fig. 8). In particular, the volume of the catalytic domain in POP is in good agreement.

However, there are also several details that are mismatched. The top part of DPPIV/CD26, which is the β-propeller in the POP structure, is clearly larger for DPPIV/CD26 (Fig.8C) and shows a central opening of diameter 18 Å, whereas the POP analogue is more compact and reveals a very small opening of only 4 Å (Fulop et al., 1998). The central cavity of DPPIV/CD26 is approximately 1.4 times larger than that of POP. The docking procedure therefore produces a position for the catalytic triad of POP misleadingly located in the cavity of DPPIV/CD26. The catalytic site of DPPIV/CD26 would, in fact, be expected to occupy a more proximal position.

The most striking difference is the second side opening in DPPIV/CD26, which is absent in POP. This new motif, taken together with the above-mentioned mismatches, leads us to speculate that the functionality of DPPIV/CD26 is most probably driven by a different mechanism from POP.

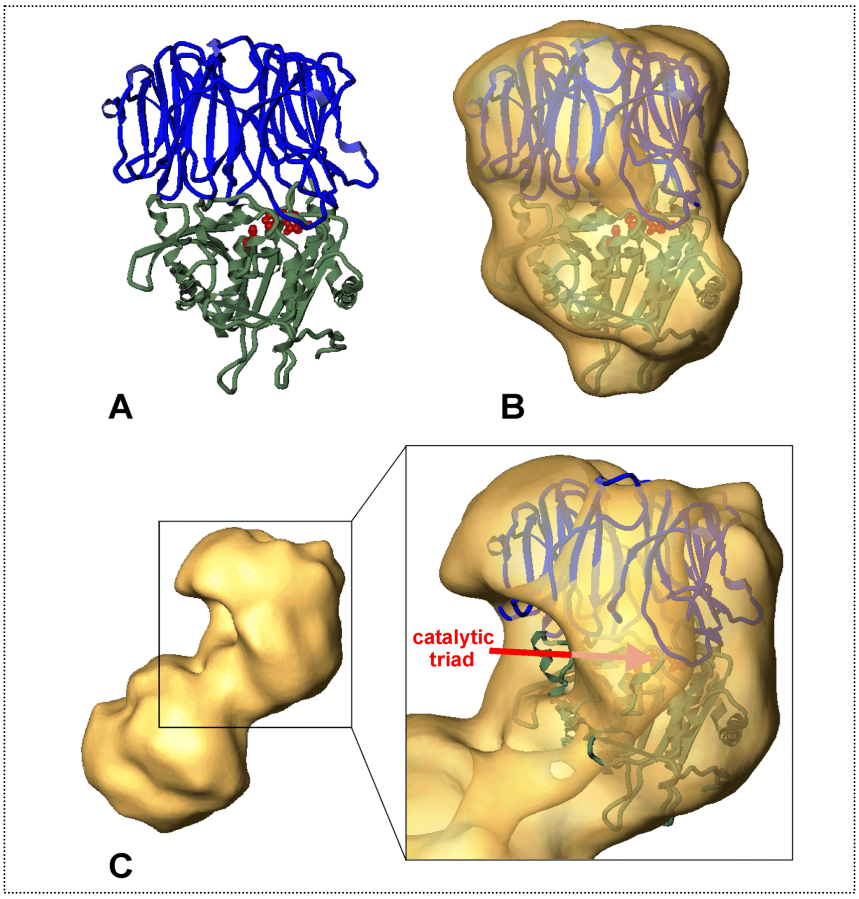

Fig.8. Crystal structure of the prolyl oligopeptidase (POP) (Fulop et al., 1998) **compared with the 3D reconstruction of rat DPPIV/CD26. A.** X-ray structure of POP (pdb-code: 1QFM): The secondary structure of the β-propeller domain and the catalytic domain are shown in blue and green, respectively. The catalytic triad (Ser^{554}, Asp^{641} and His^{680}) is represented by red balls. **B.** X-ray structure of POP as in (A) and coated by a transparent surface representation (yellow). This surface representation is the result of a low-pass filtering of the X-ray-structure and represents a resolution comparable to the EM-reconstruction (14 Å). **C.** Surface representation of the 3D reconstruction of the rat dimeric DPPIV/CD26 (left) and 3D structure of the POP (secondary structure representation) docked into one monomer of the DPPIV/CD26 density map by using "Situs" software (Wriggers and Birmanns, 2001) (right). The resulting location of the catalytic triad is indicated by an arrow.

4.2 The role of CD26 in immunoregulation

4.2.1 The expression and enzyme activity of CD26 in mouse organs and lymphocyte surface

The expression and enzyme activity of CD26 in $CD26^{-/-}$ and $CD26^{+/+}$ mouse with C57BL/6 genetic background (Marguet et al., 2000) were detected. Western blot assay confirmed there was no expression of CD26 protein in $CD26^{-/-}$ mouse, in contrast to its wide distribution in $CD26^{+/+}$ mouse. The higher expression in $CD26^{+/+}$ mouse was found in lung, liver and kidney (Fig. 9A). DPPIV activity was determined by catalytic hydrolysis of Gly-Pro-pNA chromogenic substrates (Fig. 9B). In $CD26^{-/-}$ mouse, only trace amount of enzyme activity was detected, which may be due to some unspecifically catalytic lysis by DPPIV-like enzyme. In $CD26^{+/+}$ mouse, the lung and spleen exhibited higher specific activity, which indicates a potential role of CD26 in immune system. To further analyze the surface expression of CD26 on spleen lymphocytes, FACS cytometry was performed (Fig. 9C). The spleen lymphocytes of $CD26^{-/-}$ mouse showed negative expression of CD26, while more than 90% spleen lymphocytes in $CD26^{+/+}$ mouse displayed a significant expression on cell surface.

4.2.2 CD26 deficiency modifies the distribution of murine lymphocyte sub-populations in spleen and peripheral blood

4.2.2.1 The percentage of $CD3^+$ cells is decreased, while that of NK cells is increased in spleen lymphocyte population of $CD26^{-/-}$ mice

To investigate whether CD26 expression influences the development of lymphocytes, the percentages of subsets of mouse spleen lymphocytes (MSLs) were analyzed by flow cytometry following specific mAb staining. As shown in Fig. 10, the percentage of $CD3^+$ cells in $CD26^{-/-}$ MSLs was 17% lower as compared to the values in $CD26^{+/+}$ MSLs ($30.5 \pm 4.0\%$ vs. $36.7 \pm 3.2\%$, $P<0.01$), while the percentage of $CD19^+$ cells was not significantly different between knockout and wild type mice ($57.4 \pm 3.7\%$ vs. $55.0 \pm 2.1\%$). In contrast, the proportion of spleen $NK1.1^+CD3^-$ (NK) cells was elevated by 67% in $CD26^{-/-}$ mice (4.9

± 1.5% vs. 3.0 ± 0.8%; $P<0.001$), whereas the percentage of $NK1.1^{+}CD3^{+}$ (NKT) cells was similar in MSLs of both knockout and wild type mice.

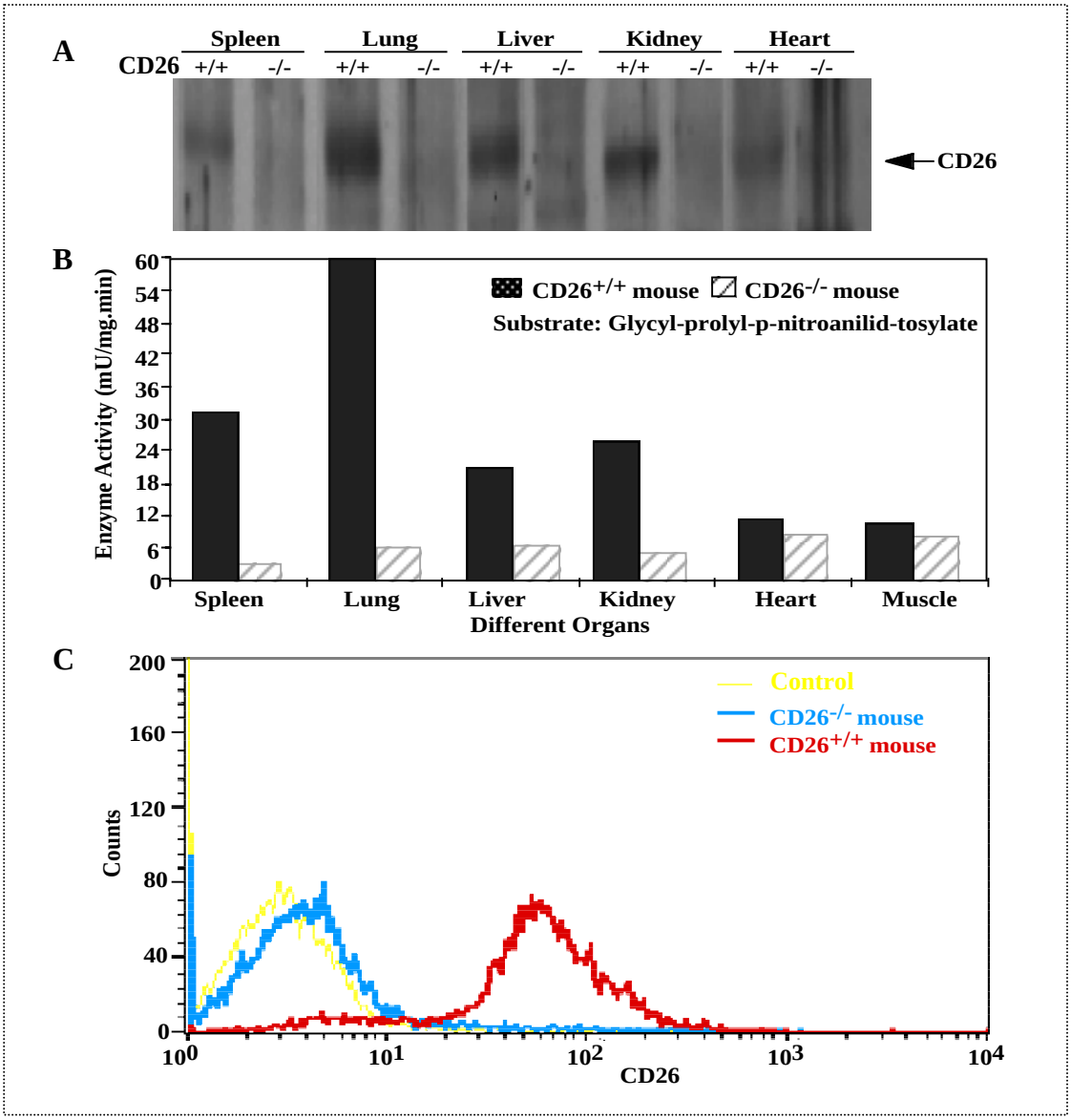

Fig. 9. Expression and distribution of CD26 in mouse organs and on lymphocyte surface. A. Western blot assay of CD26 expression in different mouse organs. Lysates of spleen, lung, liver, kidney and heart were separated on 7.5% SDS-PAGE and analyzed by Western blot. **B.** Enzyme activity analysis of organ lysates. **C.** Surface expression of CD26 on spleen lymphocytes. Spleen lymphocytes were stained with FITC-conjugated anti mouse CD26 mAb and analyzed by FACScan cytometry.

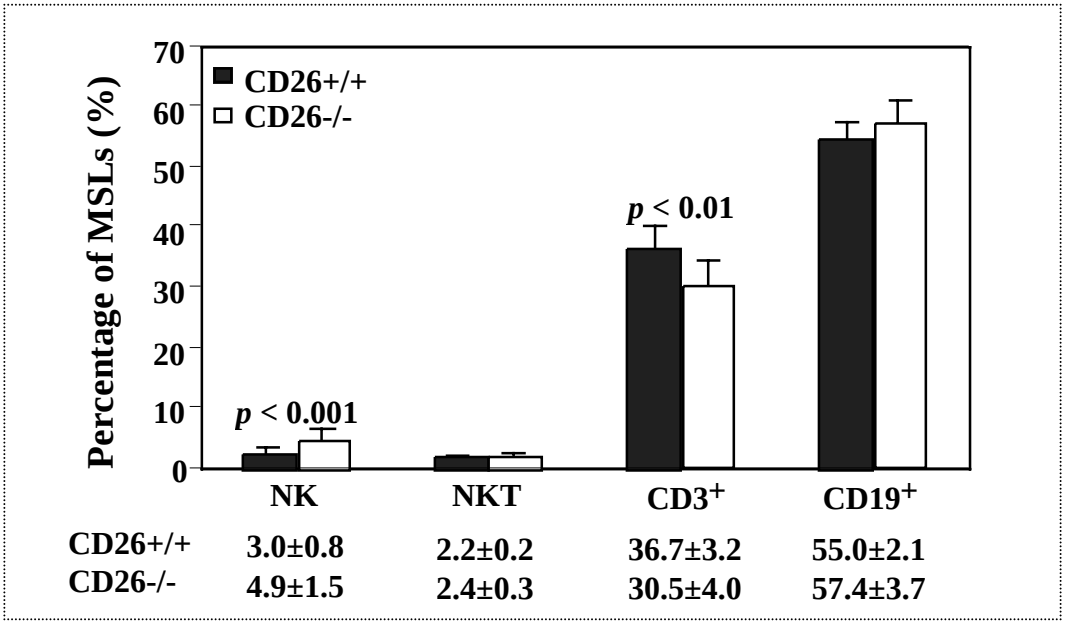

Fig. 10. Percentage of mice spleen lymphocyte subpopulations. Lymphocytes were separated and analyzed by flow cytometry as described in materials and methods. The values represent the mean ± SD of twenty mice. NK: $NK1.1^+CD3^-$, NKT: $NK1.1^+CD3^+$.

4.2.2.2 A decrease of $NK1.1^-CD4^+$ T cells contributes to the reduced proportion of $CD3^+$ population in mouse spleen lymphocytes

There are two main subsets in $CD3^+$ sub-population, $CD4^+$ and $CD8^+$ lymphocytes. As shown in Fig. 11. No difference was detected in the percentage of $CD8^+$ cells between these two kinds of mice (11.6 ± 2.1% vs. 13.2 ± 2.0%). However, the percentage of $CD4^+$ cells in MSLs of $CD26^{-/-}$ mice was decreased by 23% as compared to that in MSLs of $CD26^{+/+}$ mice (17.9 ± 2.8% vs. 23.1 ± 2.3%, $P<0.001$). Among $CD4^+$ T lymphocyte subpopulation, $CD26^{-/-}$ showed a similar percentage of $NK1.1^+CD4^+$ (NKT) cells (1.5 ± 0.4% vs. 1.5 ± 1.3%) and significant reduced $NK1.1^-CD4^+$ (conventional $CD4^+$ T) cells percentage (16.3 ± 3.3% vs. 21.2 ± 0.3%, $P<0.001$). This indicates that reduction of $CD3^+$ lymphocytes in MSLs is caused by a decrease of the conventional $CD4^+$ subset.

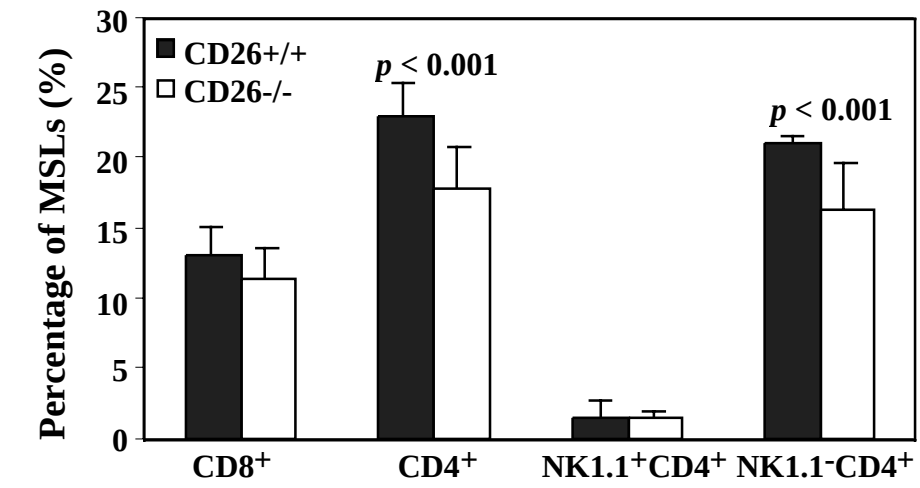

	$CD8^+$	$CD4^+$	$NK1.1^+CD4^+$	$NK1.1^-CD4^+$
CD26+/+	13.2±2.0	23.1±2.3	1.5±1.3	21.2±0.3
CD26-/-	11.6±2.1	17.9±2.8	1.5±0.4	16.3±3.3

Fig. 11. Percentage of mice spleen T lymphocyte subpopulations. Lymphocytes were separated and analyzed by flow cytometry as described in materials and methods. The values represent the mean ± SD of twenty mice.

4.2.2.3 The percentage of $CD4^+$ NKT cells is significantly lower in peripheral blood lymphocyte population of $CD26^{-/-}$ mice

Subpopulations of peripheral blood lymphocytes (PBLs) were analyzed. According to the data shown in Fig. 12, in PBLs, no difference was found in the percentages of $CD3^+$ (also two main subsets $CD4^+$ and $CD8^+$ lymphocytes), $CD19^+$, or NK cells between the two groups of mice. However, the percentage of NKT cells in $CD26^{-/-}$ mice was decreased to 40% of that in $CD26^{+/+}$ mice (6.5 ± 1.5% vs. 16.5 ± 3.0 %, $P<0.001$) (Fig. 12 and Fig. 13A). There are three subsets of NKT cells, $CD4^+$, $CD4^-CD8^-$ and $CD8^+$ NKT cells. $CD4^+$ NKT cells account for the majority. Further analysis of NKT subsets showed that the decreased NKT lymphocytes were $NK1.1^+CD4^+$ ($CD4^+$ NKT) cells, which represented only 22% of that in $CD26^{+/+}$ mice (2.7 ± 0.4% vs. 12.1 ± 1.9%; $P<0.001$) (Fig. 12 and Fig. 13B).

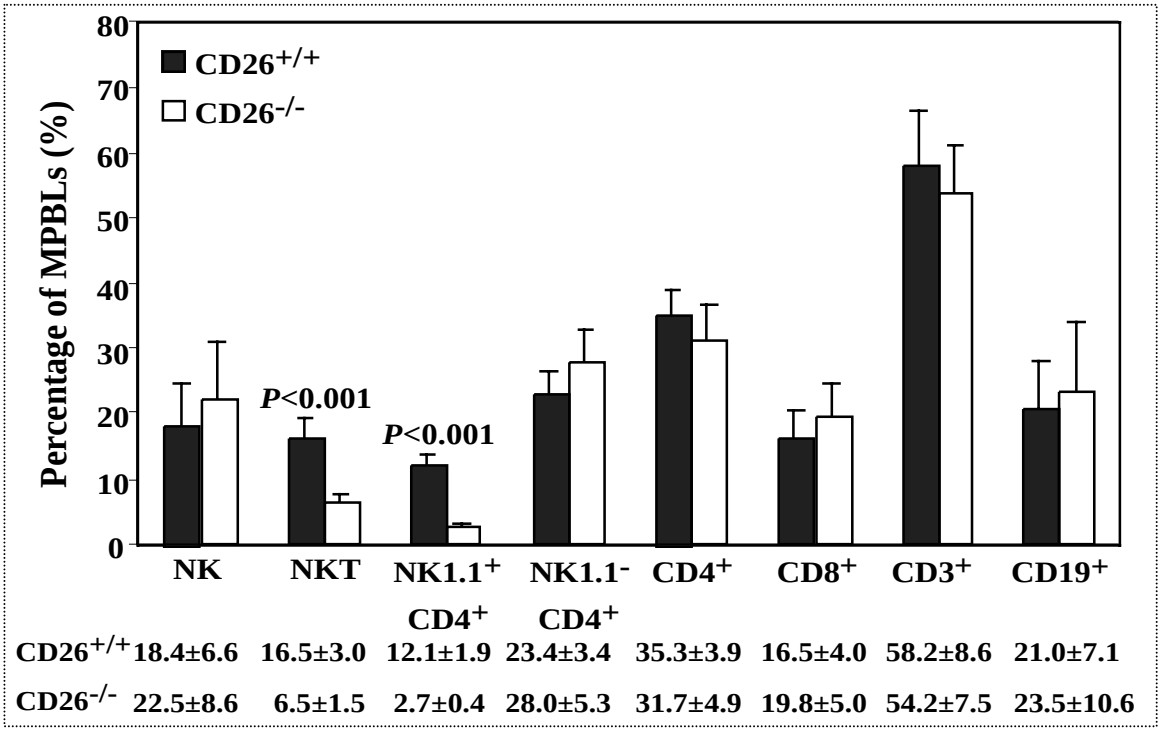

	NK	NKT	NK1.1$^+$ CD4$^+$	NK1.1$^-$ CD4$^+$	CD4$^+$	CD8$^+$	CD3$^+$	CD19$^+$
CD26$^{+/+}$	18.4±6.6	16.5±3.0	12.1±1.9	23.4±3.4	35.3±3.9	16.5±4.0	58.2±8.6	21.0±7.1
CD26$^{-/-}$	22.5±8.6	6.5±1.5	2.7±0.4	28.0±5.3	31.7±4.9	19.8±5.0	54.2±7.5	23.5±10.6

Fig. 12. Percentage of mice peripheral blood lymphocyte subpopulations. Lymphocytes were separated and analyzed by flow cytometry as described in materials and methods. The values represent the mean ± SD of seven mice. NK: NK1.1$^+$CD3$^-$, NKT: NK1.1$^+$CD3$^+$.

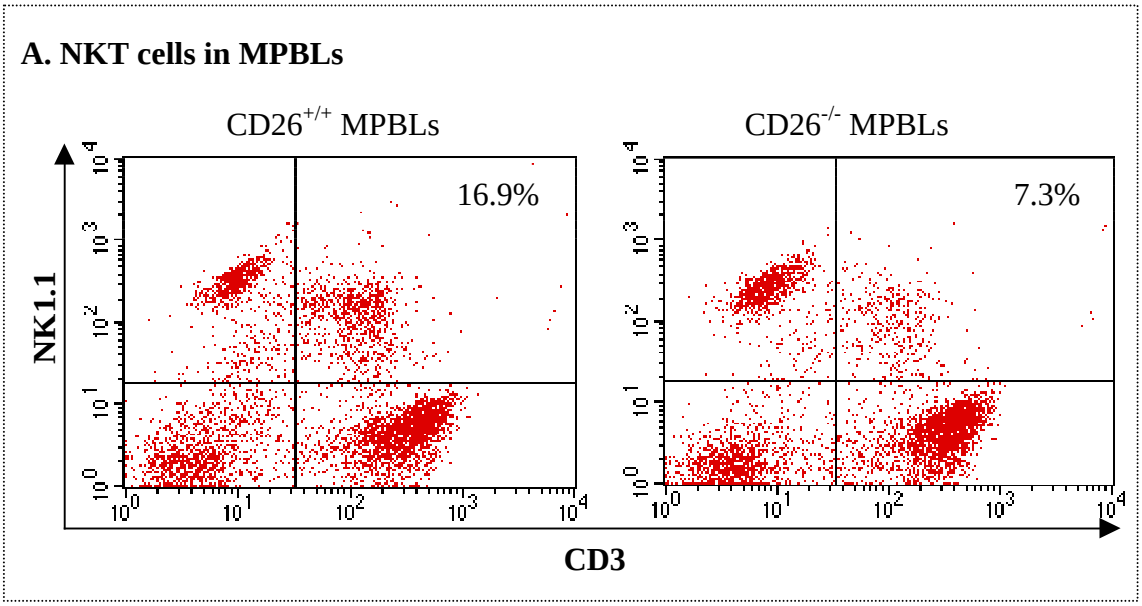

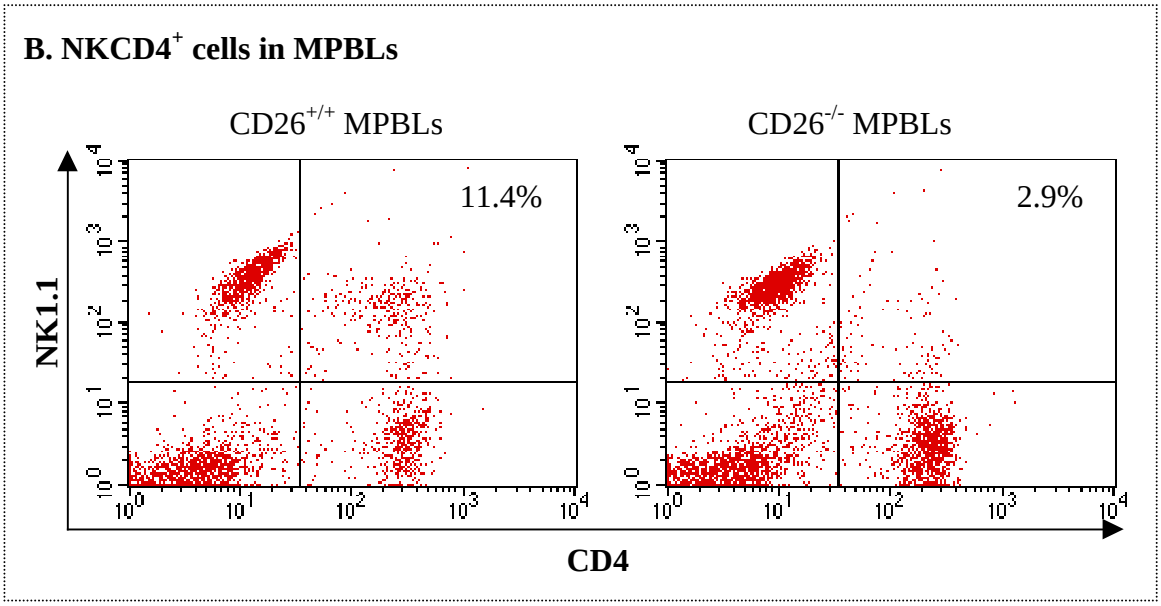

Fig. 13. Flow cytometry assay of NKT and CD4$^+$NKT cells in MPBLs populations. MPBLs were separated by density centrifugation over Ficoll separation solution and analyzed by flow cytometry as described in materials and methods. R-PE-conjugated anti-mouse NK1.1 mAb, FITC-conjugated anti-mouse CD3 mAb and FITC-conjugated anti-mouse CD4 mAb were used for immnostaining. Data were shown as one representative of seven experiments.

4.2.3 Impaired cytokine and immunoglobulin secretion of CD26$^{-/-}$ mice upon PWM stimulation

4.2.3.1 CD26 deficiency results in a decreased proliferation of mouse spleen lymphocytes after stimulation by PWM or by ConA

To examine the influence of CD26 deficiency on the immune response, MSLs from CD26$^{-/-}$ and CD26$^{+/+}$ mice were stimulated with the mitogens, PHA, PWM, ConA and LPS, respectively. The activation and proliferation of MSLs was measured by the Alamar Blue assay. No significant differences on proliferation rates were observed after stimulation with PHA or LPS, but the proliferation rates of CD26$^{-/-}$ MSLs were decreased by about 20% (P<0.05) after stimulation by PWM (182% vs. 222%) or Con A (335% vs. 442%) (Fig. 14A). Based on the proliferation curve of MSLs upon stimulation by different

concentrations of PWM or ConA (Fig. 14B), PWM 0.5 μg/ml or ConA 16 μg/ml was used to stimulate cytokine secretion of MSLs for subsequent analysis of T cell differentiation.

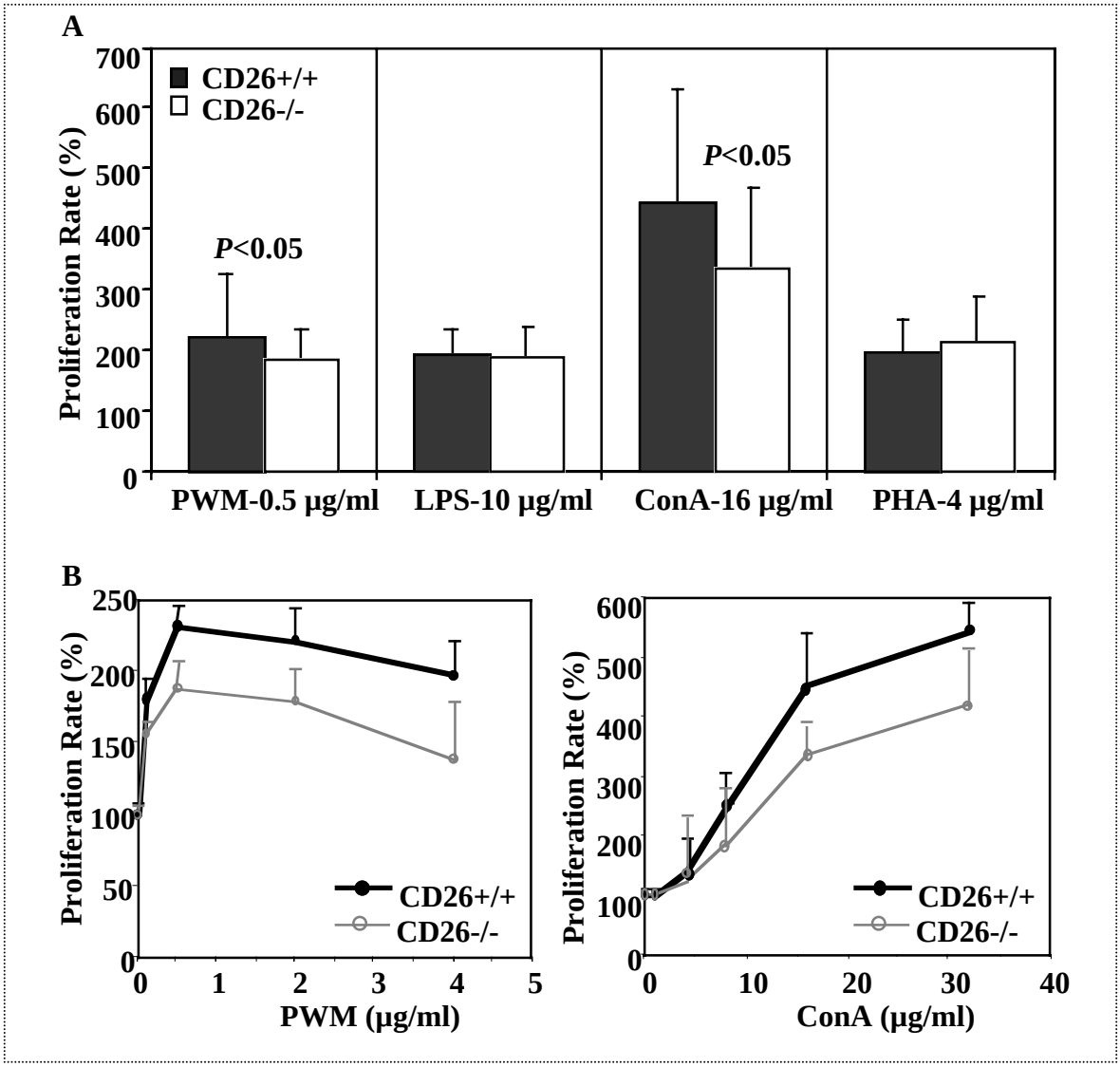

Fig. 14. Influence of CD26 deficiency on the proliferation of mouse spleen lymphocytes stimulated by different mitogens. Lymphocytes were stimulated as described in materials and methods. The proliferation rate was determined by the Alamar Blue assay. **A.** Proliferation of mouse spleen lymphocytes stimulated with different mitogens. The values represented the mean ± SD of seven mice. **B.** Proliferation of mouse spleen lymphocytes stimulated with different concentrations of PWM or ConA. Data were shown as triplicates of one of three representative experiments.

4.2.3.2 PWM is a better stimulator than ConA on IL-2 and IL-4 secretion

Based on cytokines production upon T cell activation, T helper cells can be divided into at least two subsets, Th1 and Th2. Th1 cells produce IL-2, IFN-γ and TNF β, and Th2 cells produce IL-4, IL-5, IL-6, IL-10 and IL-13. To further investigate the influence of CD26 expression on lymphocyte activation and differentiation, the cytokine production of MSLs was analyzed after stimulation *in vitro*. Compared with ConA, PWM was found to be a better stimulator on IL-2 and IL-4 secretion. The significant increase of IL-2 and IL-4 concentration was measured at 72 h after stimulation by PWM, which was much greater than those following stimulation by ConA (Fig. 15). Thus PWM was used as the stimulator during the following experiments.

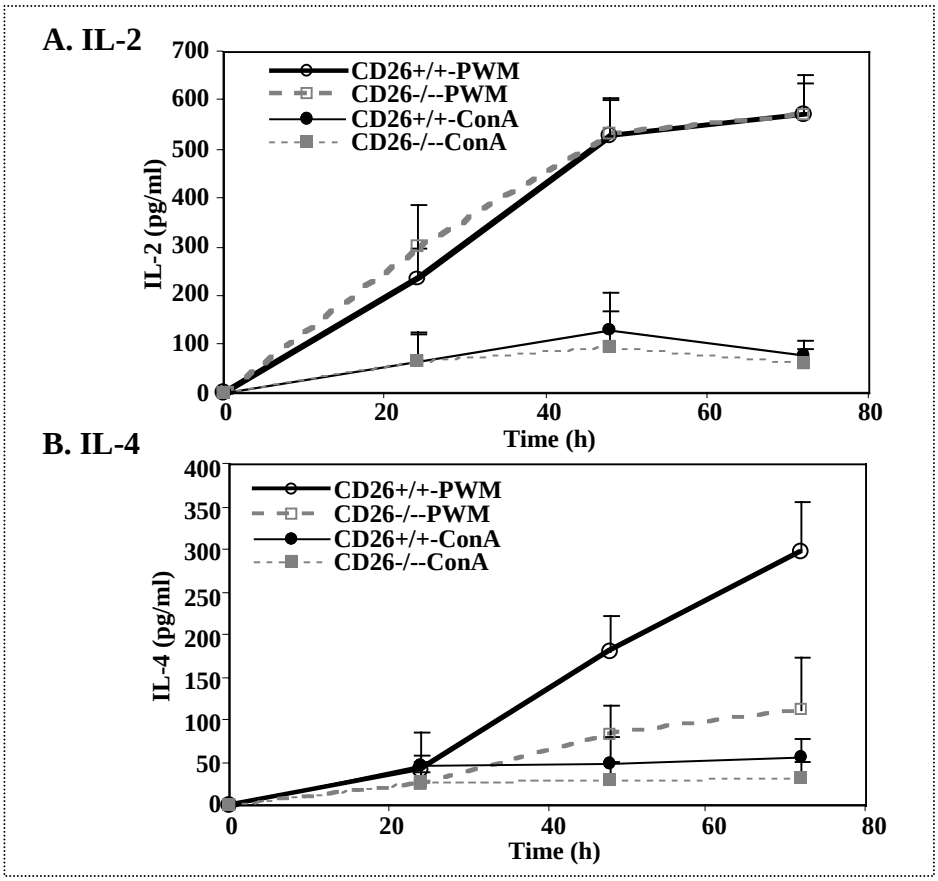

Fig. 15. PWM- and Con A- stimulated IL-2, IL-4 secretion of MSLs. A. IL-2. **B.** IL-4. MSLs were stimulated with PWM 0.5 μg/ml or ConA 16 μg/ml as described in materials and methods. Cytokine concentrations in the supernatants were measured by ELISA. The values represent the mean ± SD of a minimum of seven mice at each time point.

4.2.3.3 MSLs from CD26$^{-/-}$ mice secreted markedly less IL-4, but more IFN-γ and IL-10 after stimulation by PWM

T cell differentiation was investigated systematically based on cytokine secretion tendency upon stimulation with PWM *in vitro*. The concentrations of different cytokines in the supernatants were measured by ELISA at different times. Fig. 16 showed that stimulation with PWM resulted in an increased cytokine release into the supernatant of MSLs. IL-4 concentration reached the maximum at 72 h after stimulation. Differences between CD26$^{+/+}$ and CD26$^{-/-}$ MSLs were measured at all time points, in particular after 72 h-stimulation. At 72 and 96 h, supernatants from CD26$^{+/+}$ MSLs contained 2.5- and 3.4- fold more IL-4, respectively, than those from CD26$^{-/-}$ MSLs (403 ± 42 vs. 162 ± 71 pg/ml, P<0.001; 346 ± 31 vs. 101 ± 48 pg/ml, P<0.001, respectively) (Fig. 16 A). In contrast, CD26$^{-/-}$ MSLs produced 1.6-fold more IFN-γ and 1.4-fold more IL-10 than CD26$^{+/+}$ MSLs at 72 h after stimulation (34 ± 5 vs. 55 ± 20 µg/ml, P<0.05; 258 ± 39 vs. 363 ± 97 pg/ml, P<0.05, respectively) (Fig. 16B and C), however the magnitude of the differences was much smaller than that of IL-4 production. No significant differences were found on the production of IL-2, IL-5, IL-6 and IL-13 (Fig. 16D, E, F and G).

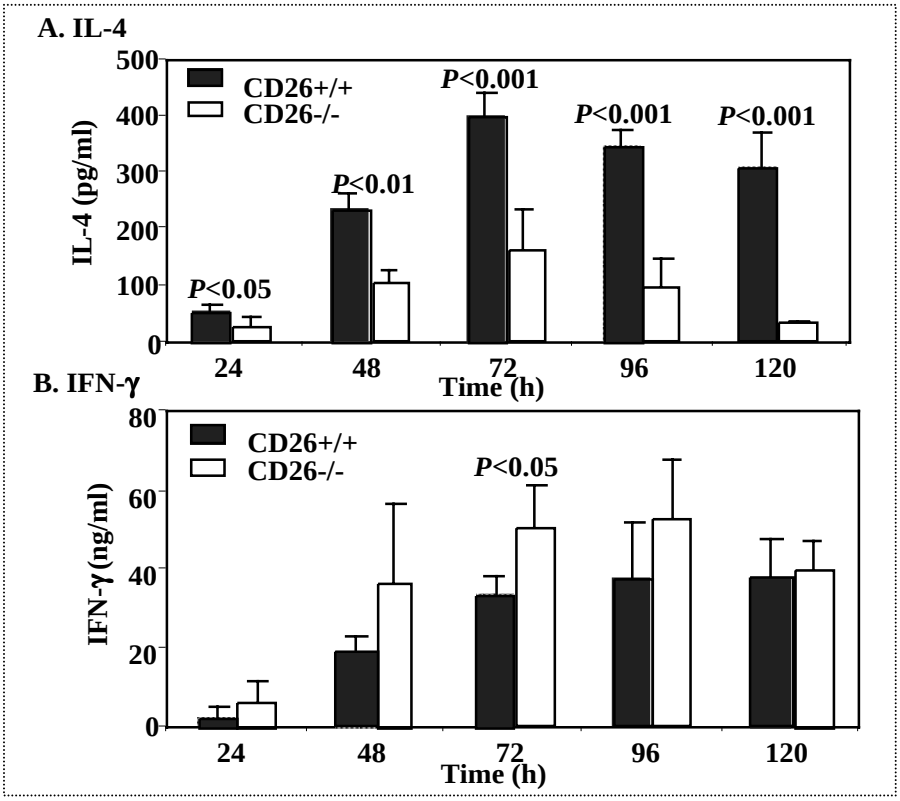

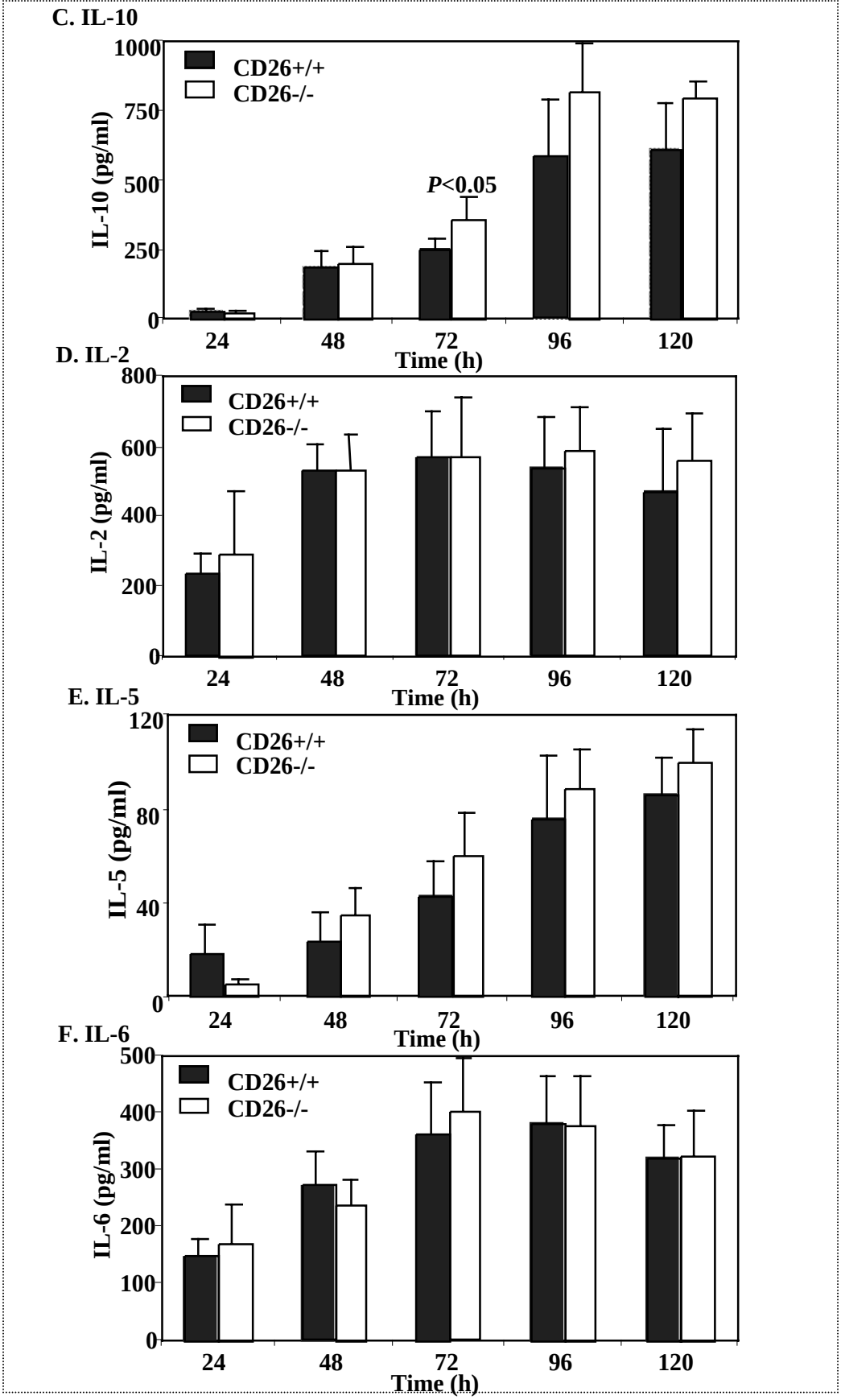
C. IL-10
IL-10 (pg/ml)
1000
750
500
250
0
CD26+/+
CD26-/-
P<0.05
24
48
72
96
120
Time (h)
D. IL-2
IL-2 (pg/ml)
800
600
400
200
0
CD26+/+
CD26-/-
24
48
72
96
120
Time (h)
E. IL-5
IL-5 (pg/ml)
120
80
40
0
CD26+/+
CD26-/-
24
48
72
96
120
Time (h)
F. IL-6
IL-6 (pg/ml)
500
400
300
200
100
0
CD26+/+
CD26-/-
24
48
72
96
120
Time (h)

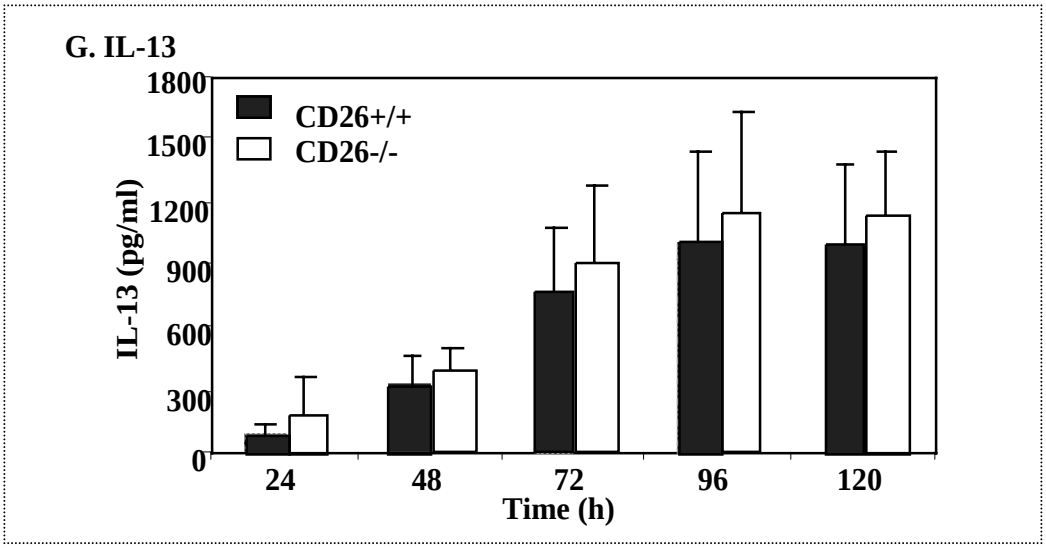

Fig. 16. Concentrations of IL-4, IFN-γ, IL-10, IL-2, IL-5, IL-6 and IL-13 in the supernatants of mouse spleen lymphocytes after stimulation by PWM. Lymphocytes were stimulated with PWM (0.5 μg/ml) as described in materials and methods. Cytokine concentrations were measured by ELISA. The values represent the mean ± SD of a minimum of seven mice at each time point.

After PWM stimulation, IL-4- and IFN-γ- producing cells were analyzed by intracellular staining and flow cytometry. Fig. 17A showed IL-4 was produced mainly by $CD4^+$ lymphocytes. The percentage of producing cells in $CD26^{+/+}$ MSLs was higher than in $CD26^{-/-}$ MSLs although the difference was not very impressive (6.52% vs. 4.34%). IFN-γ was produced by $CD4^+$ as well as $CD4^-$ lymphocytes (Fig. 17B). The percentage of IFN-γ-producing cells in $CD26^{-/-}$MSLs, including both $CD4^+$ and $CD4^-$ subpopulations, was more than their wild type counterparts. But obviously, a higher proportion of $CD4^+CD26^{-/-}$ lymphocytes secreted IFN-γ than $CD4^+CD26^{+/+}$ cells (0.89% vs. 0.49%). PWM can only stimulate few cells to produce IFN-γ, which made it difficult to further identify IFN-γ-producing cells in $CD4^-$ subpopulation.

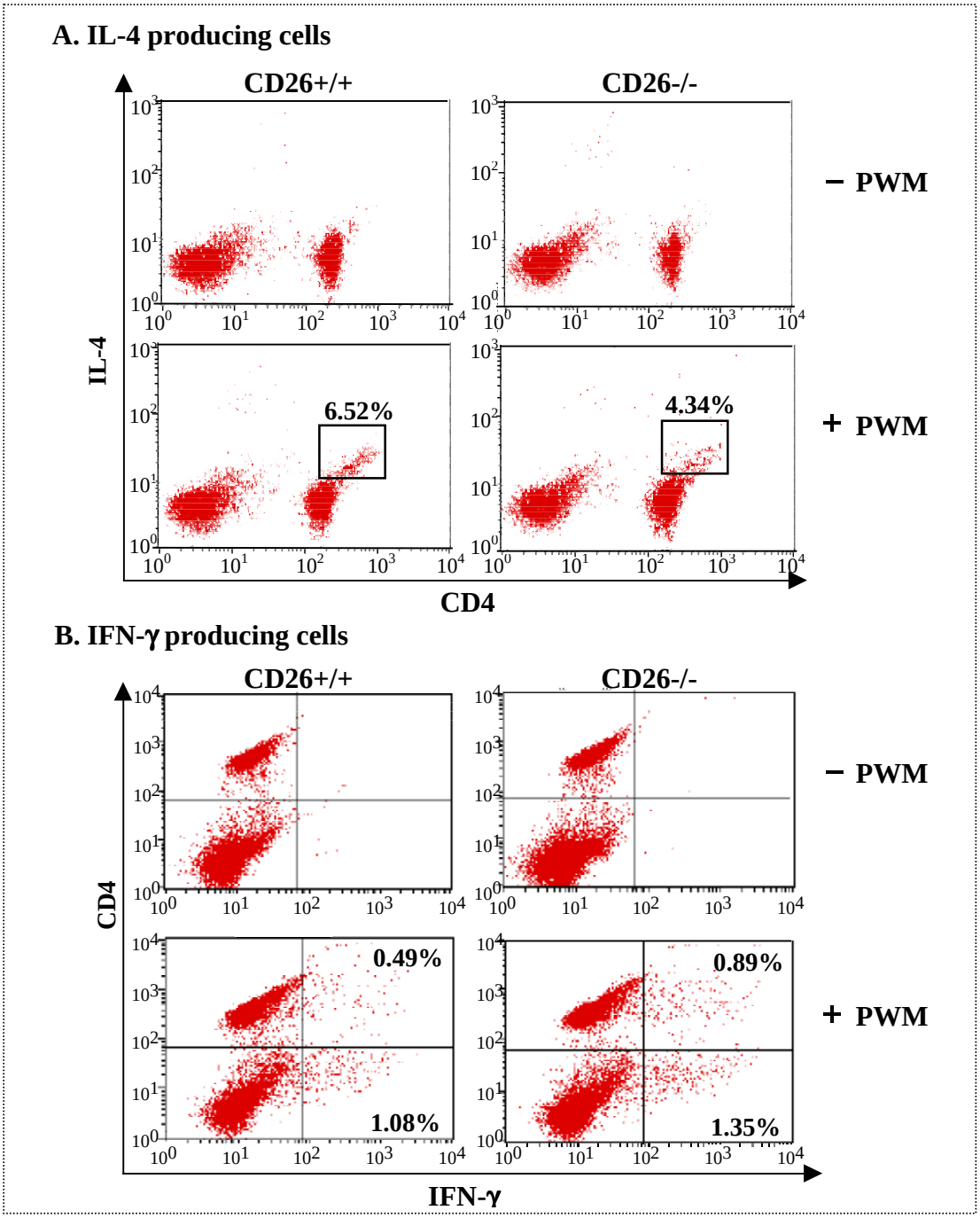

Fig. 17. IL-4 and IFN-γ producing cells in PWM-stimulated MSLs. Lymphocytes were stimulated with PWM (0.5 µg/ml) for 48 h. Monensin was added to cell culture in the final 6 h to block cytokine secretion. R-PE-conjugated anti-mouse IL-4 mAb, FITC-conjugated anti-mouse IFN-γ mAb and R-PE or FITC-conjugated anti-mouse CD4 mAb were used for immunostaining. Intracellular cytokine staining was performed as described in materials and methods. Data were shown as one representative of three experiments.

4.2.3.4 $CD26^{-/-}$ mice produced markedly less IgG after immunization by PWM

The reduced IL-4 production by $CD26^{-/-}$ MSLs prompted us to examine whether differentiation and immunoglobulin production of B lymphocyte were dependent on the expression of CD26. Mice were immunized with PWM on day 0 and day 13, and the concentrations of different immunoglobulin classes in sera were measured by ELISA at different times after immunization. Fig. 18 showed that the concentrations of IgM and IgG in sera reached a peak on days 6 and 19 after immunization. Both kinds of mice produced similar amounts of IgM at each of the indicated times (Fig. 18A). On day 6 after primary immunization the IgM concentration of both $CD26^{+/+}$ and $CD26^{-/-}$ mice increased about 2-fold, from 6000 to 12000 ng/ml and from 4750 to 9800 ng/ml, respectively. On day19 (day 6 after secondary immunization), IgM concentrations were 12000 and 12200 ng/ml, respectively. However, $CD26^{-/-}$ mice showed significantly lower IgG concentrations, especially after primary immunization (Fig. 18B). On day 6, the increment of serum IgG concentrations in $CD26^{+/+}$ mice was 1400 µg/ml (from 1700 to 3100 µg/ml), while in the sera of $CD26^{-/-}$ mice this increase was only 450 µg/ml (from 1250 to 1700 µg/ml) (Fig. 18B). The IgG increase in $CD26^{-/-}$ mice was only one third of that in $CD26^{+/+}$ mice. On day 19 (day 6 after secondary immunization), the concentrations of IgG produced by $CD26^{-/-}$ and $CD26^{+/+}$, 2280 and 2770 µg/ml, respectively, showed no marked difference. Therefore, deficiency of CD26 resulted in a decreased IgG production after primary immunization, but it did not result in decreased IgM production.

4.2.3.5 CD26 deficiency impaired B cell immunoglobulin isotype switching to IgG1, IgG2a and IgE upon treatment by PWM

To further examine whether CD26 deficiency influences immunoglobulin isotype switching of B cells, the production of IgG1, IgG2a and IgE was measured at different time points after immunization of mice with PWM. As shown in Fig. 19, the concentrations of all these antibodies were significantly lower in $CD26^{-/-}$ mice. Until day 6 after primary immunization, IgG1 production in $CD26^{-/-}$ mice increased barely (Fig. 19A). And IgG2a production elevated slightly (65 µg/ml, from 153 ± 60 to 218 ± 56 µg/ml) (Fig. 19B), in comparison with $CD26^{+/+}$ mice which showed marked increases in IgG1 and

IgG2a production (491 µg/ml, from 325 ± 158 µg/ml to 816 ± 476 µg/ml; and 236 µg/ml, from 199 ± 54 µg/ml to 435 ± 184 µg/ml, respectively). After second immunization, increases of IgG1 and IgG2a production in sera of $CD26^{-/-}$ mice were detectable, but it was still less than in $CD26^{+/+}$ mice. Following the stimulation, the production of IgE was increased and reached a peak at day 19 after immunization. The maximal concentration of serum IgE in $CD26^{-/-}$ mice was lower than in $CD26^{+/+}$ mice (715 ± 144 ng/ml and 1123 ± 82 ng/ml) (Fig. 19C). Therefore, CD26 deficiency impaired B cell immunoglobulin isotype switching to IgG1, IgG2a and IgE after treatment by PWM.

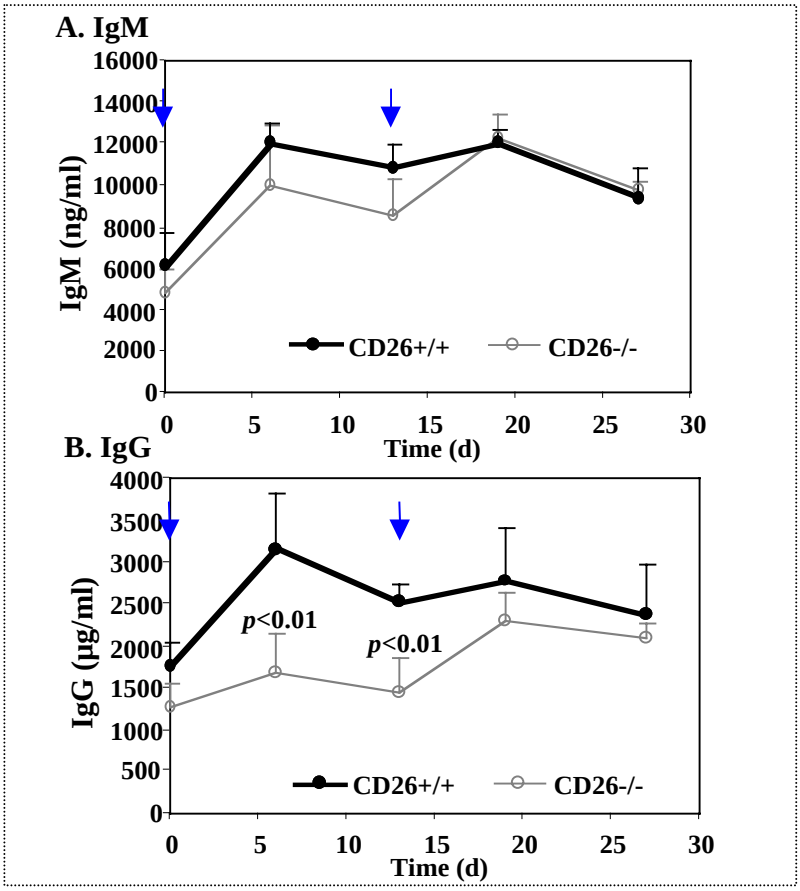

Fig. 18. Concentrations of IgM and IgG in the sera of mice after immunization with PWM. Mice were immunized twice on day 0 and 13 (40 µg/mouse, ip.), respectively as described in materials and methods. Blood was taken at the indicated times. IgM and IgG concentrations in sera were analyzed by ELISA. The values represented the mean ± SD of a minimum of five mice at each time point. Time points for intraperitoneal injection were indicated by arrows.

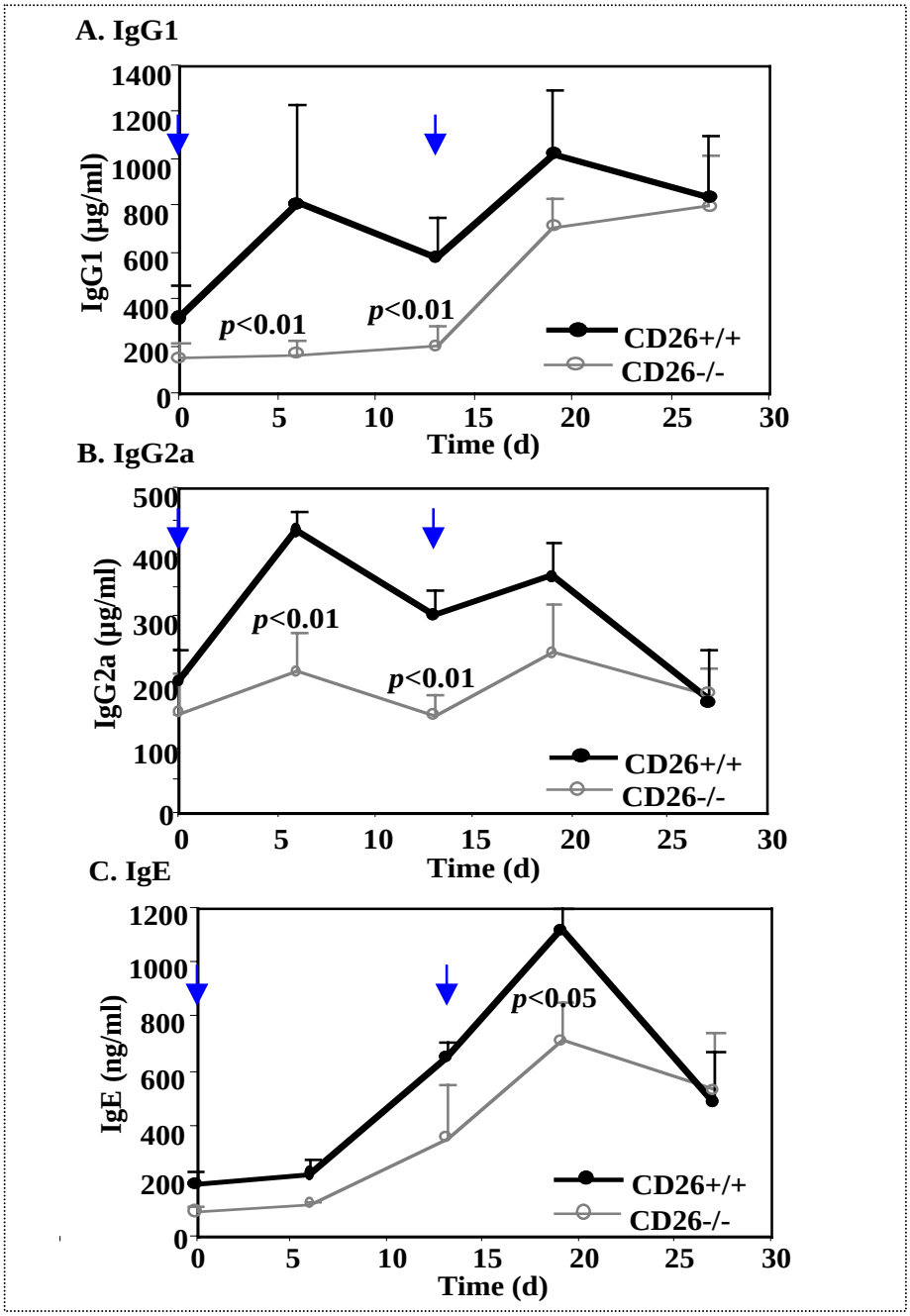

Fig. 19. Concentrations of IgG1, IgG2a and IgE in the sera of mice after immunization with PWM. Mice were immunized twice on day 0 and 13 (40 µg/mouse, ip.), respectively as described in materials and methods. Blood was taken at the indicated times. IgG1, IgG2a and IgE concentrations in sera were analyzed by ELISA. The values represent the mean ± SD of a minimum of five mice at each time point. Time points for intraperitoneal injection were indicated by arrows.

4.2.3.6 Reduced IL-4, IL-2, and delayed IFN-γ production in sera of CD26$^{-/-}$ mice immunized by PWM

The lower IgG production as well as the impaired immunoglobulin isotype switching in CD26$^{-/-}$ mice triggered us to determine the concentrations of different cytokines in sera after immunization by PWM. According to the cytokine production of MSLs *in vitro* (Fig. 16) and immunoglobulin secretion in sera (Fig. 18 and 19), Th1 cytokines IL-2 and IFN-γ, Th2 cytokines IL-4 and IL-5 were measured. All of these four cytokines contribute to B cell activation, proliferation and differentiation to plasma cells and involved in immunoglobulin secretion and isotype switching. As shown in Fig. 20, injection of PWM induced a rapid elevation of these cytokines in sera. IL-2, IL-4, IL-5 and IFN-γ concentrations peaked at 2 h, 4 h, 4 h and 12 h after immunization, respectively. All these cytokines dropped down to basic level after 36 h upon immunization (data not shown). In sera of CD26$^{-/-}$ mice the maximal value of IL-4 was 38% (182 ± 91 vs. 471 ± 77 pg/ml, $P<0.01$), and that of IL-2 about 50% (395 ± 70 vs. 794 ± 121 pg/ml, $P<0.05$) of that in CD26$^{+/+}$ mice (Fig. 20C and A). The maximum of IFN-γ production was not affected, however, a delayed IFN-γ increase was observed in CD26$^{-/-}$ mice. At 2 h after immunization, CD26$^{-/-}$ mice secreted only half the amount of IFN-γ as compared with CD26$^{+/+}$ (210 vs. 409 pg/ml, $P<0.05$) (Fig. 20B). No significant difference was observed in IL-5 production (Fig. 20D).

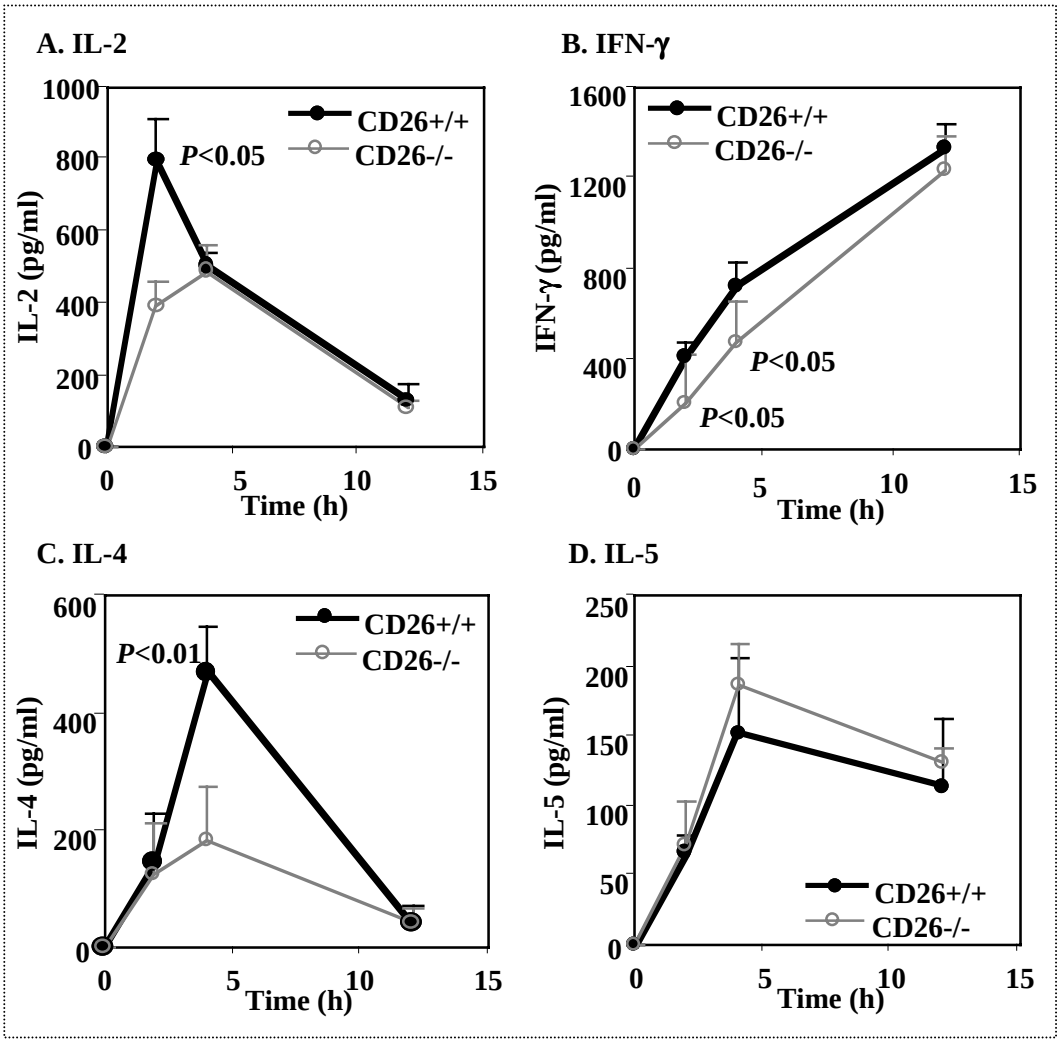

Fig. 20. Concentrations of IL-2, IFN-γ, IL-4 and IL-5 in mice sera after stimulation by PWM. Mice were immunized on day 0 (40 μg/mouse, ip.) as described in materials and methods. Blood was taken at the indicated times. Cytokine concentrations were measured by ELISA. The values represented the mean ± SD of six mice at each time point.

4.2.4 Impaired immunoglobulin secretion and enhanced lung inflammation in CD26$^{-/-}$ mice upon ovalbumin immunization

4.2.4.1 CD26$^{-/-}$ mice produced less IgM and markedly less IgG after OVA immunization

Mice were sensitized with ovalbumin (OVA) on day 0 and day 5, and challenged by aerosol OVA on day 12. The concentrations of different immunoglobulin classes in sera were measured at different times after immunization by ELISA. Fig. 21 showed that concentrations of both IgM and IgG in sera of CD26$^{-/-}$ mouse were lower as compared with CD26$^{+/+}$ mouse. On day 5 and 10, sera from CD26$^{+/+}$ mice contained 1.4-fold more IgM than those from CD26$^{-/-}$ MSLs (160 vs. 114 μg/ml, P<0.01 and 273 vs. 192 μg/ml, P<0.05 respectively) (Fig. 21A). While, the differences of IgG concentrations between these two strains (Fig. 21B) were more significant than IgM on statistics. On day 5, there was still nearly no increase on IgG concentration in both strains. Following the second sensitization, increment of serum IgG concentrations was detectable. On day 10 and 13, CD26$^{+/+}$ mouse produced 1.5-fold more IgG than CD26$^{-/-}$ mouse (3042 vs. 2097 μg/ml, P<0.00001 and 3888 vs. 2532 μg/ml, P<0.001 respectively).

4.2.4.2 CD26 deficiency impaired B cell immunoglobulin isotype switching to IgG1, IgG2a, but not IgE upon immunization by OVA

Immunoglobulin isotype switching of B cells was determined for OVA immunization based on the production of IgG1, IgG2a and IgE. Mice were immunized with OVA as described above. As shown in Fig. 22, the concentrations of two subclasses, IgG1 and IgG2a, were significantly lower in CD26$^{-/-}$ mice. On day 10 and 13 after primary immunization, sera from CD26$^{+/+}$ mice contained 1.7- and 2.3-fold more IgG1 than those from CD26$^{-/-}$ MSLs (1436 vs. 849 μg/ml, P<0.01 and 2164 vs. 922 μg/ml, P<0.0001) (Fig. 22A). The difference on IgG2a production was exhibited as early as day 5 (Fig. 22B). On the days 5, 10 and 13, respectively, IgG2a concentrations in sera of CD26$^{+/+}$ mice were 2.2-, 2.7- and 2.0-fold more than that in CD26$^{-/-}$ mice (650 vs. 290 μg/ml, P<0.05, 1126 vs. 411 μg/ml, P<0.0001 and 1337 vs. 652 μg/ml, P<0.001), respectively. However, unlike the

response to PWM stimulation, there was no significant difference found on IgE production between both kinds of mice after OVA immunization although the maxima of IgE concentration were reached on day 10 (Fig. 22C).

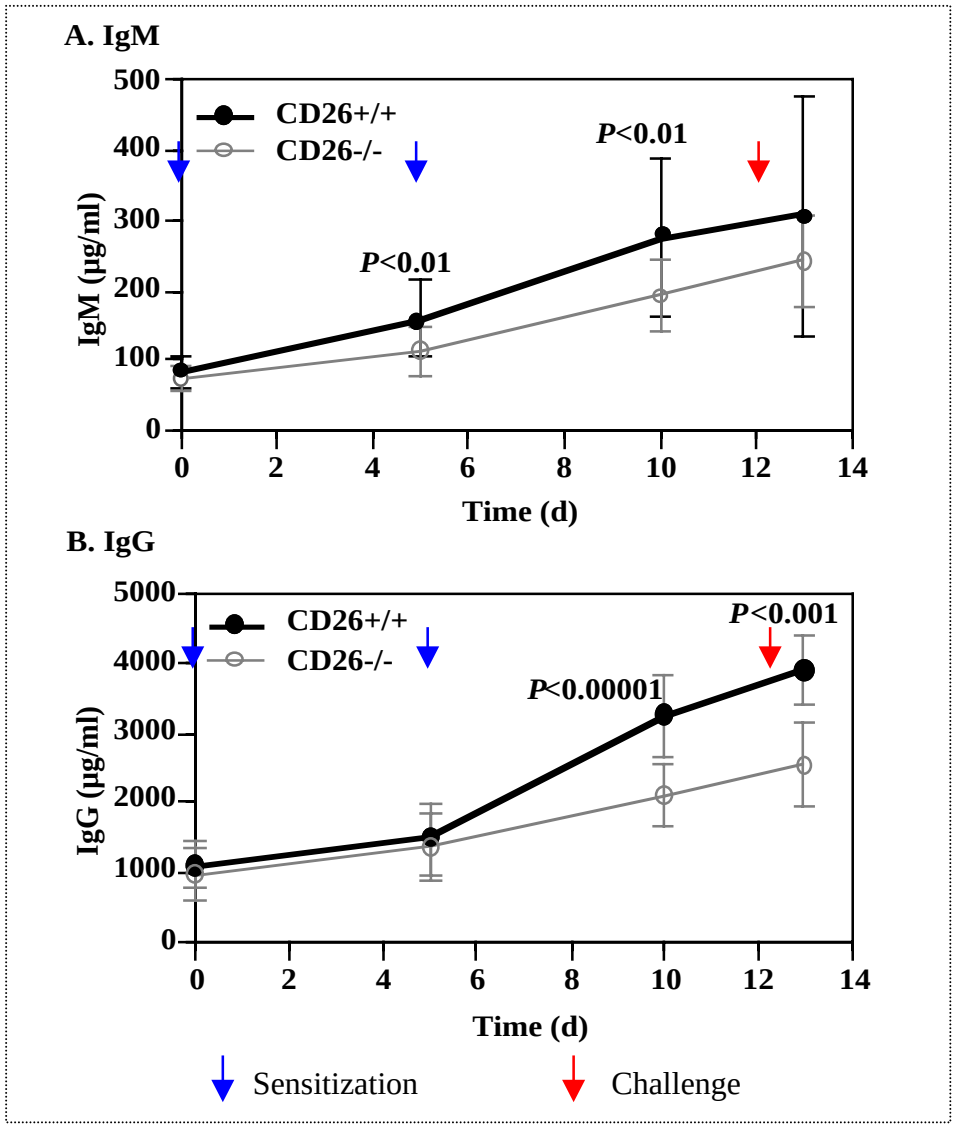

Fig. 21. Concentrations of IgM and IgG in the mouse sera after OVA immunization. Mice were immunized twice on day 0 and 5 (20 µg/mouse, ip.), respectively and challenged (1% OVA in endotoxin free PBS for 40 min) on day 12 as described in materials and methods. Blood was taken at the indicated times. IgM and IgG concentrations in sera were analyzed by ELISA. The values represented the mean ± SD of fourteen mice at each time point.

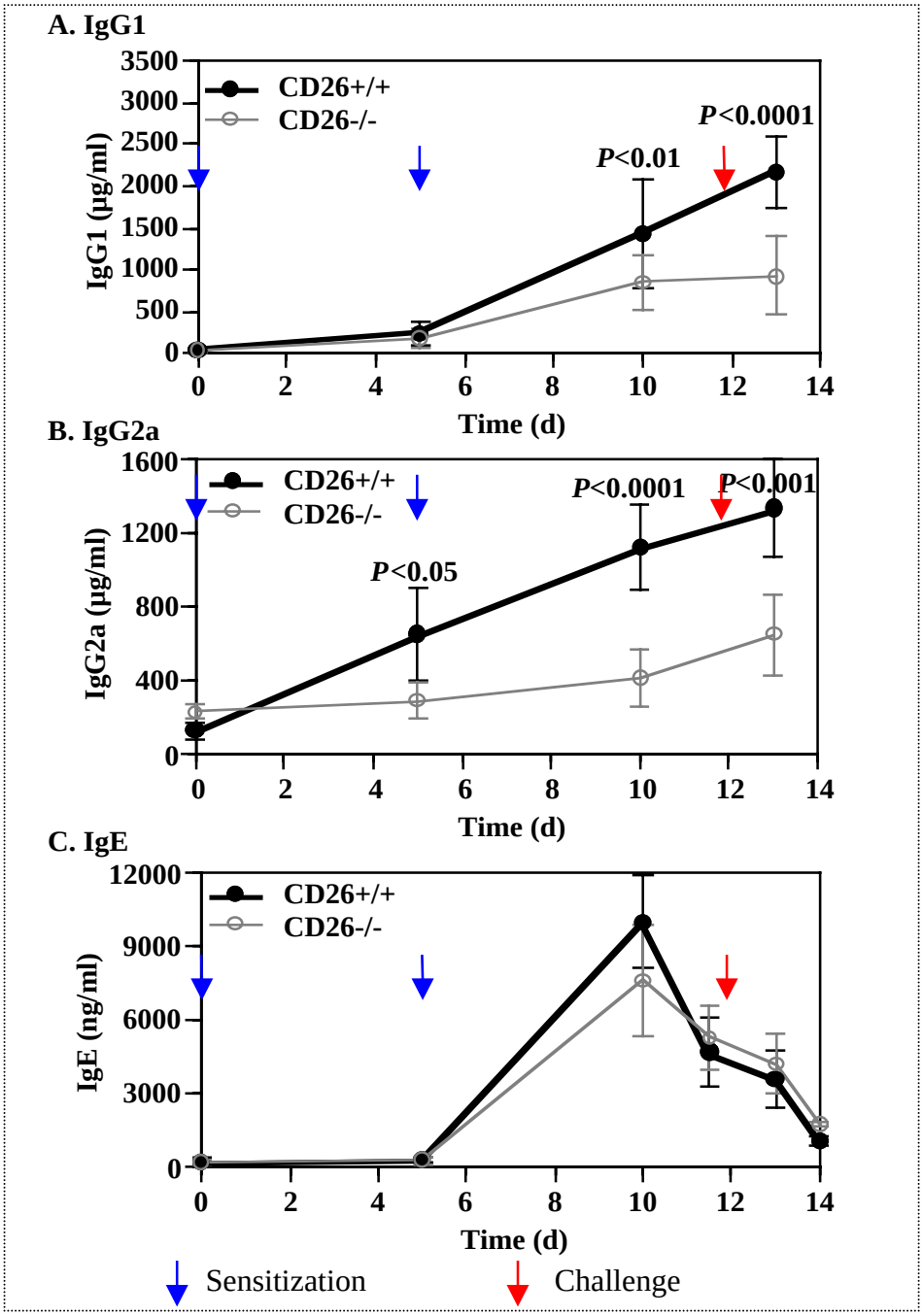

Fig. 22. Concentrations of IgG1, IgG2a and IgE in the sera of mice after immunization with OVA. Mice were immunized twice on day 0 and 5 (20 µg/mouse, ip.), respectively and challenged (1% OVA in endotoxin free PBS for 40 min) on day 12 as described in materials and methods. Blood was taken at the indicated times. IgG1, IgG2a and IgG concentrations in sera were analyzed by ELISA. The values represented the mean ± SD of fourteen mice at each time point.

4.2.4.3 Severe antigen-induced eosinophilic airway inflammation in the lungs of $CD26^{-/-}$ mice

OVA-induced airway hyperresponsiveness is an animal model of asthma. The clinical hallmarks include reversible airway abstruction, chronic airway inflammation and non-specific airway hyperresponsiveness. The early phase is characterized by IgE production and mast cell degranulation. The late phase is associated with eosinophils and T cell recruitment (Lukacs, 2001). Therefore, besides measurement of immunoglobulin production in mice sera, the airway inflammation was assessed by histological techniques.

Mice were killed at 36 h after aerosol challenge with OVA and the lungs were sectioned at –20°C and stained with hematoxylin & eosin. As shown in Fig. 23, OVA challenge of both kinds of mice provoked a peribronchiolar and perivascular inflammatory response (Fig. 23C and D), which was not seen in animals sham-sensitized with Alu-Gel-S suspension (Alum, Serva) and challenged with PBS (Fig. 23A and B). However, compared with $CD26^{+/+}$ mice, $CD26^{-/-}$ mice showed markedly enhanced tissue response (Fig. 23C and D). Denser pulmonary infiltrates containing eosinophils around vessels and in the parenchyma were observed in $CD26^{-/-}$ mice (Fig. 23D and F). A micrograph of the eosinophils in bronchoalveolar lavage fluid (BALF) of $CD26^{-/-}$ mice was shown in Fig. 23E.

The impressive difference in lung inflammation between these two kinds of mice was also observed in BALF recovered from the animals. (Fig. 24). BAL was performed at 36 h after aerosol OVA challenge. Cytospin preparations of BAL cells were stained with Giemsa & May-Grünwald solution and cell differentiation were enumerated based on morphology and staining profile. OVA sensitization and challenge caused an impressive increase in BAL cellularity and eosinophils proportion in both kinds of mice. According with tissue response, this increase is more predominant in $CD26^{-/-}$ mice. The total cell numbers in the BALF from $CD26^{-/-}$ mice was 5-fold higher than in the BALF derived from $CD26^{+/+}$ mice ($4.5 \pm 1.2 \times 10^6$ vs. $0.96 \pm 0.8 \times 10^6$ cells per lung) (Fig. 24A). Eosinophils consisted of the majority of BALF cellularity in $CD26^{-/-}$ mice. The percentage of eosinophils in BALF of $CD26^{+/+}$ and $CD26^{-/-}$ mice is 42% and 72% respectively (Fig. 24).

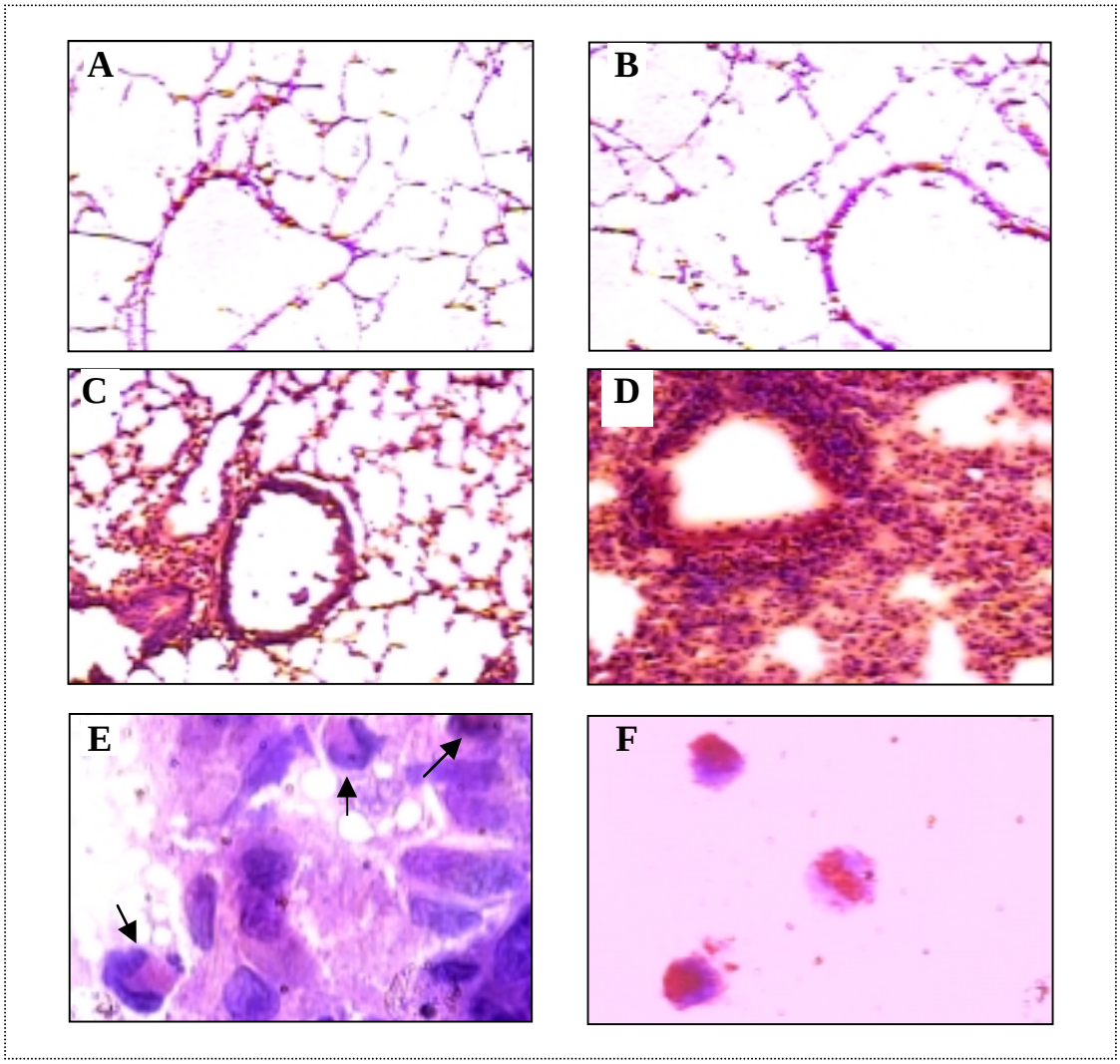

Fig. 23. OVA induced airway inflammation in CD26$^{-/-}$ and CD26$^{+/+}$ mice. Mice were immunized twice on day 0 and 5 and challenged on day 12 as described in materials and methods. Lung tissue and BALF were obtained at 36 h after challenge. Lung sections were stained with H&E and cytospin preparations of BAL cells were stained with Giemsa & May-Grünwald solution. **A & B.** Lung sections of Alum/PBS-treated CD26$^{+/+}$ mouse (A) and CD26$^{-/-}$ mouse (B) (100 x magnification). **C & D.** Lung sections of OVA-Alum/OVA-treated CD26$^{+/+}$ mouse (C) and CD26$^{-/-}$ mouse (D) (100 x magnification). **E.** Lung sections of OVA-Alum/OVA-treated CD26$^{-/-}$ mouse (1000 x magnification). Eosinophils in the inflammation sites are indicated by arrows. **F.** Eosinophils in the BALF of OVA-Alum/OVA-treated CD26$^{-/-}$ mouse (1000 x magnification).

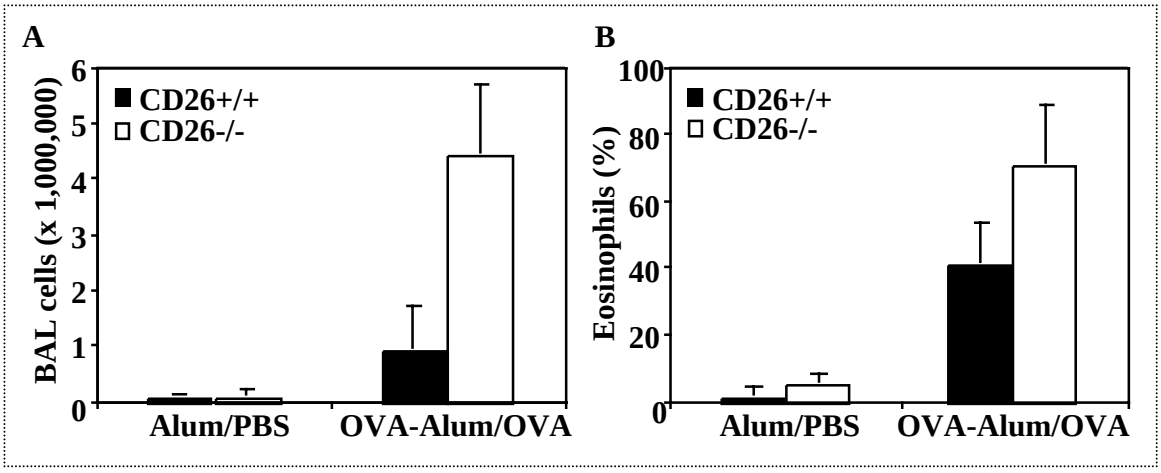

Fig. 24. Cellularity and eosinophilia in BALF. Mice were immunized twice on day 0 and 5, and challenged on day 12 as described in materials and m. BALF was obtained at 36h after challenge. The live cells recovered were counted in a hemocytometer. Cytospin preparations of BALF cells were stained with Giemsa & May-Grünwald solution. Cell differential were enumered based on morphology and staining profile. **A.** Cellularity in BALF. **B.** Percentage of eosinophils in total cells of BALF. The values represented the mean ± SD of four mice for each group.

4.2.4.4 Th2 cytokines in the lungs of OVA sensitized and challenged mice

Overwhelming evidence indicates that Th2 cytokines play a crucial role in asthmatic inflammation. Among them, IL-4 acts as the major factor regulating IgE production by B cells, and is required for optimal Th2 differentiation; IL-5, a key factor for eosinophilia, regulates most aspects of eosinophil behavior, such as growth, apoptosis, adhesion and secretion, and could therefore be responsible for some characteristics of the tissue damage; IL-13 has many actions similar to those of IL-4, but it is more active in regulating airway hypersensitivity and mucus hypersecretion. Therefore, the expression of cytokine mRNA in the lung and the concentrations of cytokine protein in BALF were measured after OVA challenge.

RT-PCR was performed to analyze the expression of different cytokine genes. Cytokine mRNA was absent in mice without exposure to aerosol OVA. After challenge with OVA,

IL-2, IL-10 and IFN-γ mRNAs were still not detectable, whereas mRNAs of IL-4, IL-5, IL-12p40 and IL-13 increased in both kinds of mice. In consitstent with severe eosinophilia in the lung of $CD26^{-/-}$ mouse, the mRNA expression of Th2 cytokines, IL-4, IL-5 and IL-13, was quite higher in $CD26^{-/-}$ mouse compared to $CD26^{+/+}$ mouse; while that of IL-12, one classic Th1 promoting cytokine, was similar in both strains. Accordingly, enhanced secretion of IL-4 and IL-5 protein was measured in BALF of $CD26^{-/-}$ mice. At 24 h after aerosol exposure, BALF of $CD26^{-/-}$ mice contained 2.1-fold more IL-4 and 2.5-fold more IL-5 than that of $CD26^{+/+}$ mice (17.6 ± 10.2 vs. 37.9 ± 10.0 pg/ml and 51.8 ± 31.5 vs. 127.5 ± 51 pg/ml, respectively) (Fig. 25B). This result indicates that increased secretion of Th2 cytokines in local sites contributes to OVA induced eosinophilia and severe inflammation response in the lung of $CD26^{-/-}$ mice.

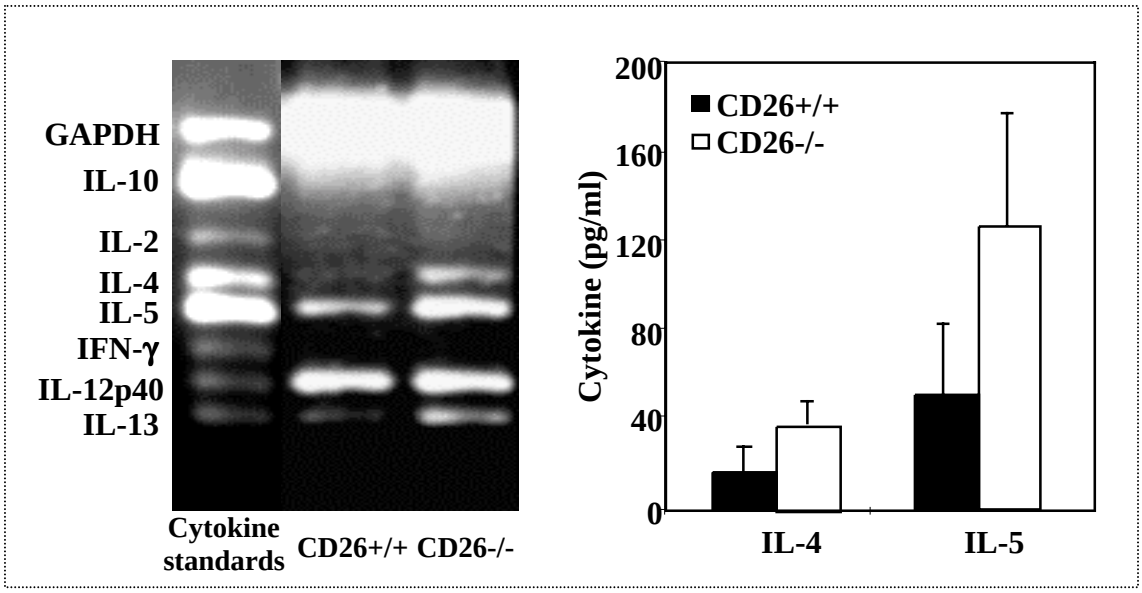

Fig. 25. Enhanced mRNA expression and protein secretion of Th2 cytokines in the lung of $CD26^{-/-}$ mouse upon OVA challenge. Mice were immunized twice on day 0 and 5 (20 μg/mouse, ip.), respectively and challenged (1% OVA in endotoxin free PBS for 40 min) on day 12 as described in materials and methods. Lung tissues and BALF were obtained at 24 h after challenge. **A.** Cytokine mRNA expression in the lung. Total RNA was isolated from mouse lung. RT-PCR was used to analyze mRNA expression. **B.** Cytokine concentrations in BALF measured by ELISA. The values represented the mean ± SD of four mice for each group.

4.2.5 Investigation on mechanisms of CD26 functions in immune system

4.2.5.1 Specific inhibitor Ile-Pro-thiazolidide inhibited the proliferation of $CD26^{+/+}$ MSLs, and exogenous CD26 with enzymatic activity increased the proliferation of $CD26^{-/-}$ MSLs upon PWM stimulation

In order to clarify how far the enzymatic activity is involved in immunoregulation, we applied the specific inhibitor of CD26/DPPIV in wild type system and the exogenous CD26 with enzymatic activity in knock out system.

Ile-Pro-thiazolidide is a specific inhibitor of DPPIV enzyme activity. As shown in Fig. 26, at 0.5 and 1 mM concentrations, it inhibited PWM-stimulated proliferation of $CD26^{+/+}$ MSLs by 28% and 42% (from 221% to 162% and 135%), respectively. It is worth mentioning that a weak inhibition was also found in both $CD26^{-/-}$ MSLs and unstimulated MSLs. At the concentration of 1 mM, this inhibitor inhibited unstimulated $CD26^{+/+}$ and $CD26^{-/-}$ MSLs by 20% and 10%, respectively.

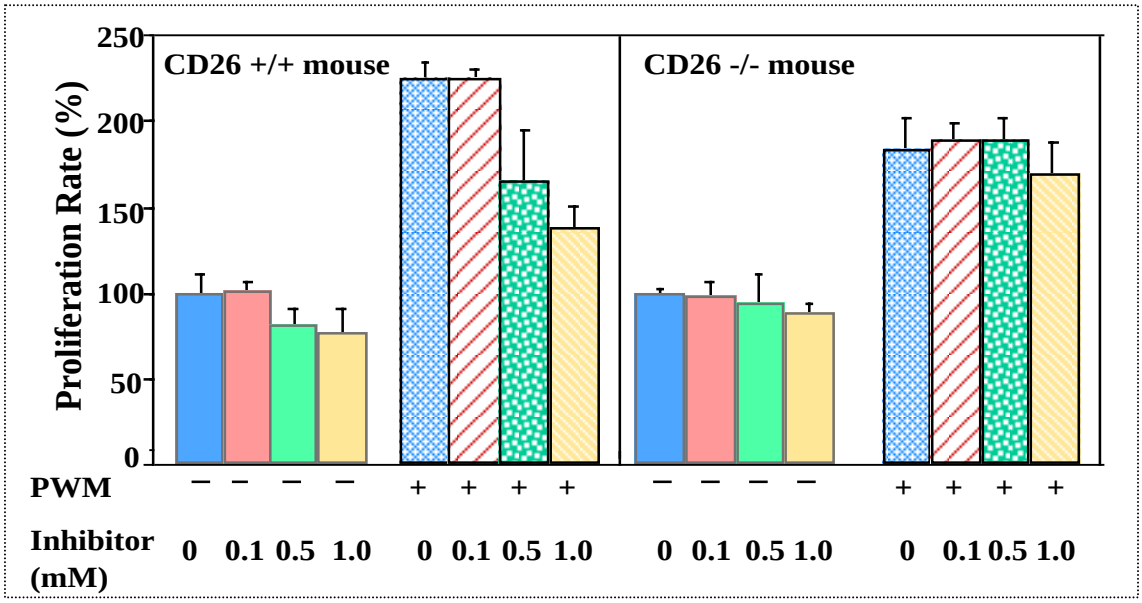

Fig. 26. Influence of specific inhibitor of DPPIV on PWM-stimulated proliferation of MSLs. Inhibitor Ile-Pro-thiazolidide was added to cell culture with or without PWM (0.5 g/ml) at the beginning of incubation. Proliferation was measured after 72 h-stimulation. Data were shown as triplicates of one representative experiment.

Rat CD26 with enzyme activity was isolated and purified from CHO/CD26 transfectants (Fig. 2). To determine its influence on the proliferation of MSLs, rat CD26 was added to MSLs culture with or without PWM stimulation. The exogenous CD26 obviously enhanced PWM-stimulated proliferation of $CD26^{-/-}$ MSLs (Fig. 27). Following addition of rat CD26, proliferation rates were increased by 17% and 44% (from 182% to 215% and 265%) at concentration of 1 and 3 μg/ml, respectively. While no effect was detected on $CD26^{+/+}$ MSLs.

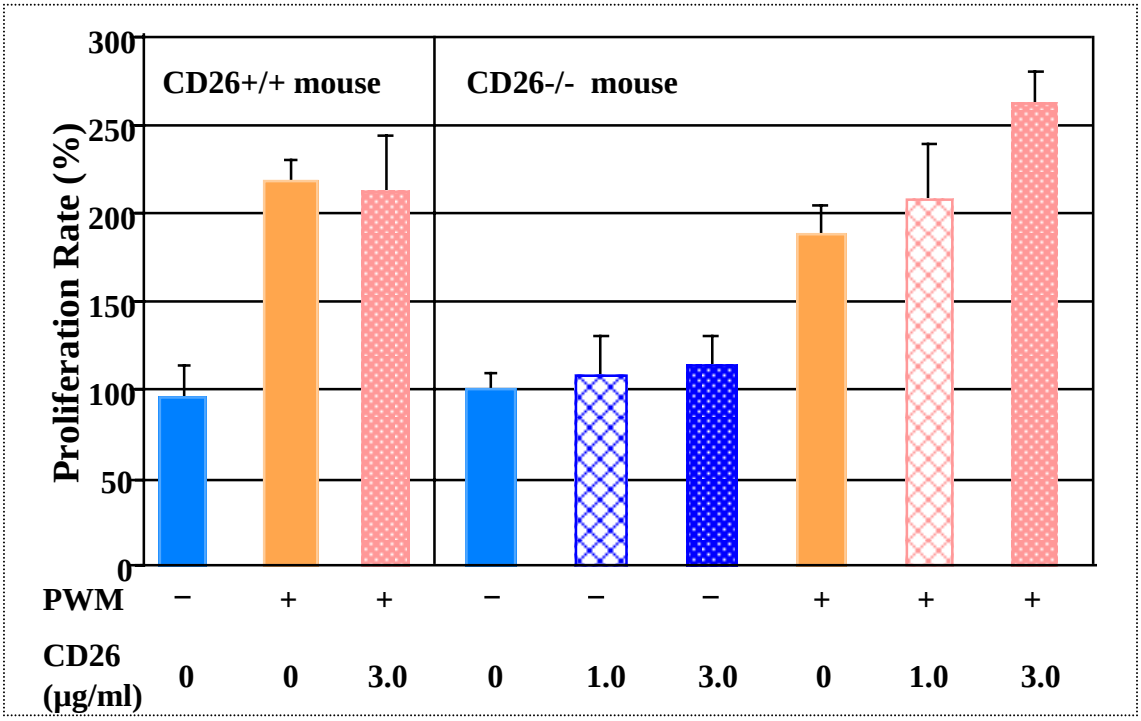

Fig. 27. Influence of exogenous rat CD26 on PWM-stimulated proliferation of MSLs. Enzymatically active rat CD26 separated and purified from CHO/CD26 cells was used as exogenous CD26, which was added to cell culture with or without PWM (0.5 μg/ml) at the beginning of incubation. Proliferation was measured at 72 h. Data were shown as triplicates of one representative experiment.

These results demonstrate the enzyme activity, at least, partially involved in lymphocyte activation and proliferation. But some unspecific inhibition should be carefully considered when inhibitor is applicated.

4.2.5.2 Ile-Pro-thiazolidide inhibited not only secreting of IL-4, but also producing of IFN-γ, IL-2 and IL-6 from PWM-stimulated MSLs

Cytokine production from Ile-Pro-thiazolidide treated MSLs was measured due to its inhibitory effect on PWM-stimulated proliferation of $CD26^{+/+}$ MSLs. Similar to the results from knock out mice (Fig. 16), Ile-Pro-thiazolidide mainly inhibited IL-4 secretion; however, different from that, it inhibited other cytokine production as well (Fig. 28). The inhibition of IL-4 and IL-2 production was dose-dependent. The highest inhibitions were 36% and 19%, respectively (Fig. 28A and B). With respect to IFN-γ and IL-6 production, low concentration of inhibitor (0.1 mM) did not inhibit and even increased production of these two cytokines slightly. While higher concentration of inhibitor exhibited strong inhibition (at 1 mM, 54% and 25%, respectively) (Fig. 28C and D).

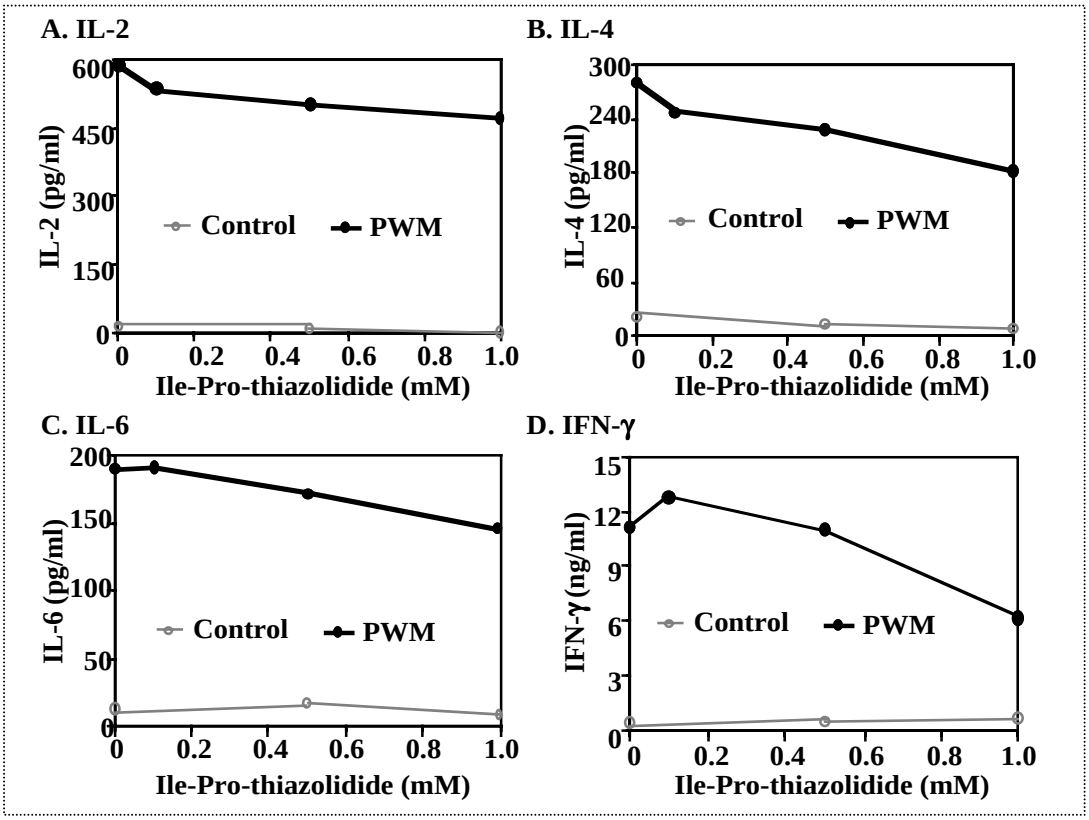

Fig. 28. Influence of DPPIV inhibitor on PWM-stimulated cytokine production of MSLs. Ile-Pro-thiazolidide combined with or without PWM (0.5 µg/ml) was added at the beginning of culture. Supernatants were harvested at 72 h. cytokine concentration was measured with ELISA. One representative of three experiments was shown.

4.2.5.3 Influence of CD26 deficiency on cytokine secretion of purified $CD4^+$ cells uopn PWM stimulation

$CD4^+$ cells were isolated from mouse spleen lymphocytes using $CD4^+$ MicroBeads and MiniMACS column. After purification, the percentage of $CD4^+$ T cells was more than 95% as detected by flow cytometry (Fig. 29). The remaining cells were non-CD4 cells. The cell viability was greater than 95% as determined by trypan blue exclusion.

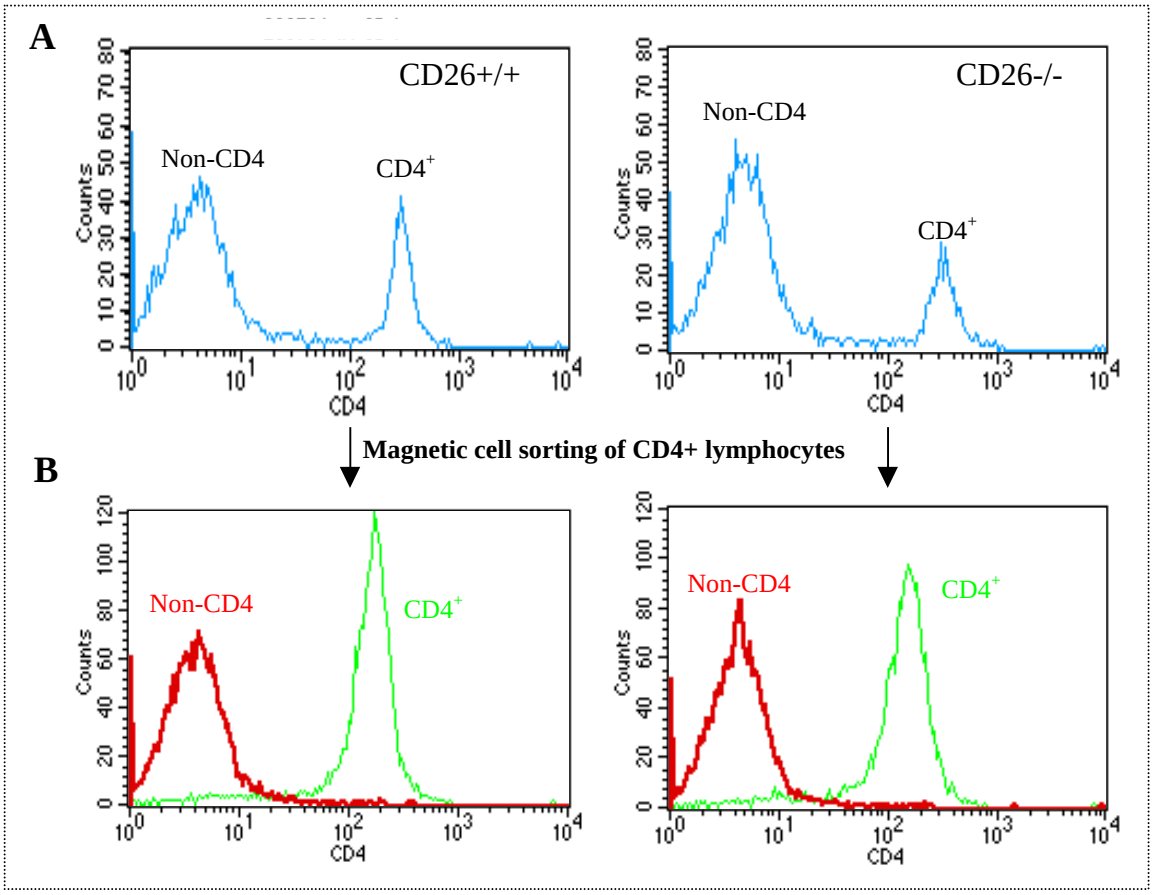

Fig. 29. Separation of CD4+ lymphocytes from MSLs by MACS. A. Flow cytometry analysis of $CD4^+$ cells in MSLs. **B.** Flow cytometry analysis of purified $CD4^+$ cell. $CD4^+$ lymphocytes were separated from MSLs by using MACS CD4 MicroBeads and MiniMACS with positive selection column.

Fig. 30 showed the cytokine production of PWM-stimulated $CD4^+$ cells. $CD26^{-/-}CD4^+$ cells secreted much more IFN-γ, IL-4, IL-6 and IL-10 than $CD26^{+/+}$ $CD4^+$ cells upon PWM

stimulation. At 72 h, $CD26^{-/-}$ $CD4^{+}$ lymphocytes produced 3.2-fold more IFN-γ (23 ng/ml vs. 7.2 ng/ml), 1.5-fold more IL-4 (2750 pg/ml vs. 1800 pg/ml), 1.5-fold more IL-6 (405 pg/ml vs.275 pg/ml), and 2.0-fold more IL-10 (1000 pg/ml vs. 500 pg/ml). Only IL-2 produced by $CD26^{-/-}$ $CD4^{+}$ cells decreased to 61% of $CD26^{+/+}$ $CD4^{+}$ cells (480 pg/ml vs. 780 pg/ml).

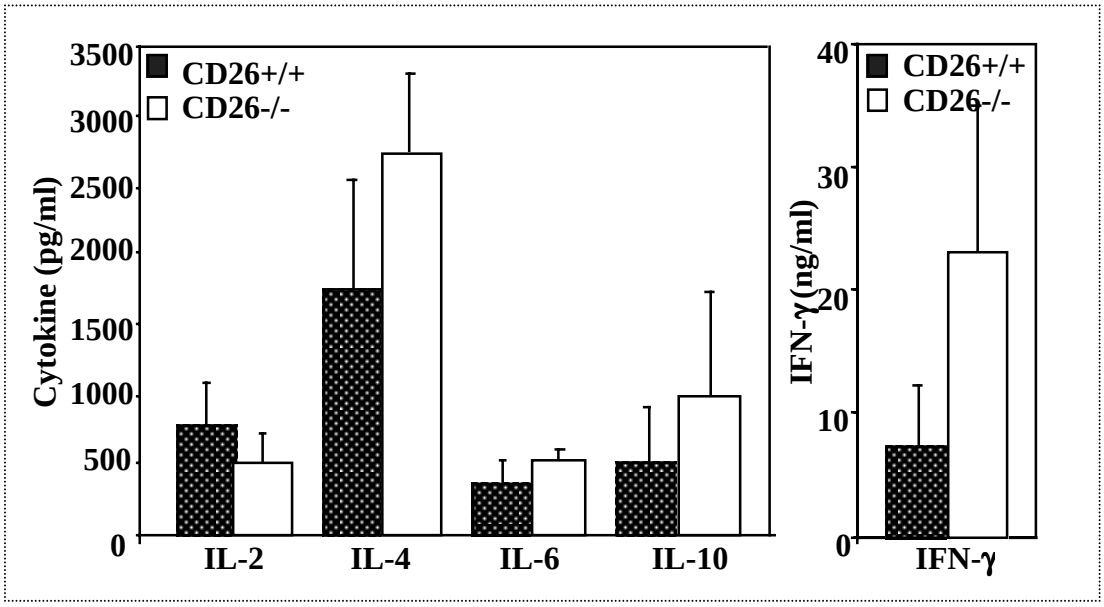

Fig. 30. Concentrations of IL-4, IFN-γ, IL-10, IL-2 and IL-6 in the supernatants of mouse $CD4^{+}$ lymphocytes after stimulation by PWM. $CD4^{+}$ lymphocytes were separated from MSLs using MACS CD4 MicroBeads and MiniMACS with positive selection column. $CD4^{+}$ lymphocytes were stimulated by PWM. (0.5 μg/ml) for 72 h. Cytokine concentrations in supernatants were measured by ELISA. The values represented the mean ± SD of a minimum of four mice.

4.3 Establishment of inducible expression system of CD26/GFP fusion protein in Jurkat cells

In our laboratory, rat CD26 cDNA was transfected into human T-cell leukemia line Jurkat cells, which do not express endogenous detectable amounts of CD26. However, what hindered the study is that stable Jurkat transfectants of CD26 reduced and lost its CD26 expression during the process of culture. Recently it is demonstrated that the expression of CD26 is involved in apoptosis of Jurkat cells (Ohnuma et al., 2002) (Aytac et al., 2001). Therefore, for studying the underlying molecular mechanisms of CD26 function, it is necessary to establish an inducible expression system of CD26 in Jurkat cells.

Tet-on gene expression system (Clontech) regulates the expression of the target protein in a reversible and dose-dependent manner under doxycycline control. This system includes a pTet-on plasmid, which is able to express a regulatory protein (rtTA), and a response plasmid, which expresses a gene of interest under control of tetracycline (Tet)-response element (TRE). In the absence of doxycyline, the regulatory protein (rtTA) is silent and does not bind the TRE; otherwise rtTA binds the TRE and activates transcription in the presence of doxycycline. When doxycyline is removed from the culture medium, transcription from TRE is turned off (Fig. 31). In the present study, we tried to create a double stable Tet-on cell line that contains both the regulatory (pTet-on) and response plasmid (pTRE2/CD26/GFP).

Furthermore, in order to simplify the analysis of expression level and location of CD26 in Jurkat cells, the fusion protein of CD26/GFP was first constructed. pEGFP-N1 encodes a red-shifted variant of wild-type GFP, which has been optimized for brighter fluorescence and higher expression in mammalian cells. Fusion of proteins to the N terminus of EGFP retains the fluorescent properties of the native EGFP protein allowing the localization of the fusion protein *in vivo* and direct expression analysis by fluorescence microscopy or FACS cytometry.

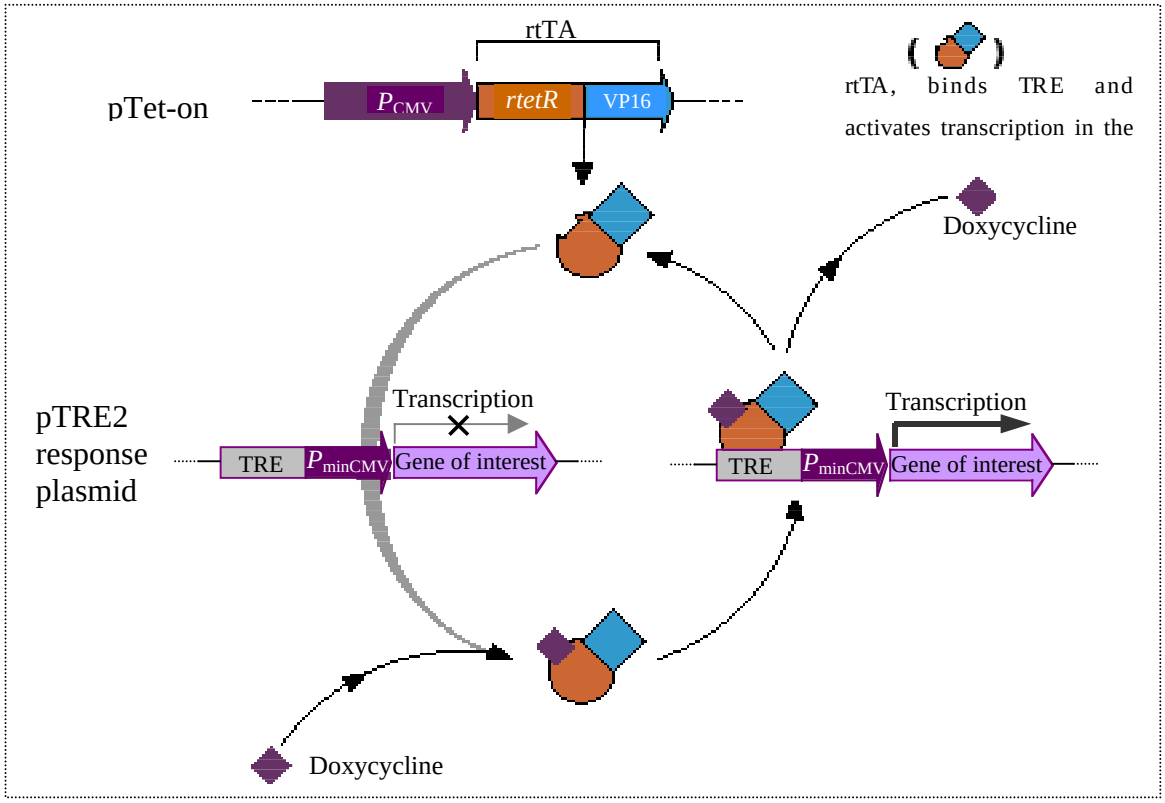

Fig. 31. Schematic diagram of gene expression regulation in the Tet-on system (Clontech). pTet-on encodes the reverse tet-controlled transcriptional activator (rtTA) from the strong immediate early promoter of cytomegalovirus (P_{CMV}). The response plasmid pTRE2 contains a Tet-responsive element (TRE) located upstream of the minimal immediate early promoter of cytomegalovirus (P_{minCMV}) which is silent in the absence of activation. In the presence of doxycycline, rTetR domain of rtTA binds the TRE and activates transcription. As doxycycline is removed from the culture medium, transcription from the TRE of pTRE2 is turned off.

4.3.1 Construction and expression of CD26/GFP fusion protein

Construction of CD26/GFP fusion protein was shown in Fig. 32. The pF-162 contains vector plasmid pRc/CMV and cDNA encoding rat CD26. In this plasmid stop codon of CD26 gene is mutated into *Sal* I endonuclease digestion site, which is unique in CD26 gene. Both plasmid pF-162 and pEGFP-N1 were treated with *Hind* III and *Sal* I. The fragment containing CD26 gene from pF-162 was then inserted into corresponding

position in multiple cloning sites (MCS) immediate upstream of GFP gene in pEGFP-N1. After ligation, CD26 gene is in the same reading frame as GFP and there are no intervening stop codons between CD26 and GFP genes. The constructed fusion protein is characterized by both CD26 and GFP.

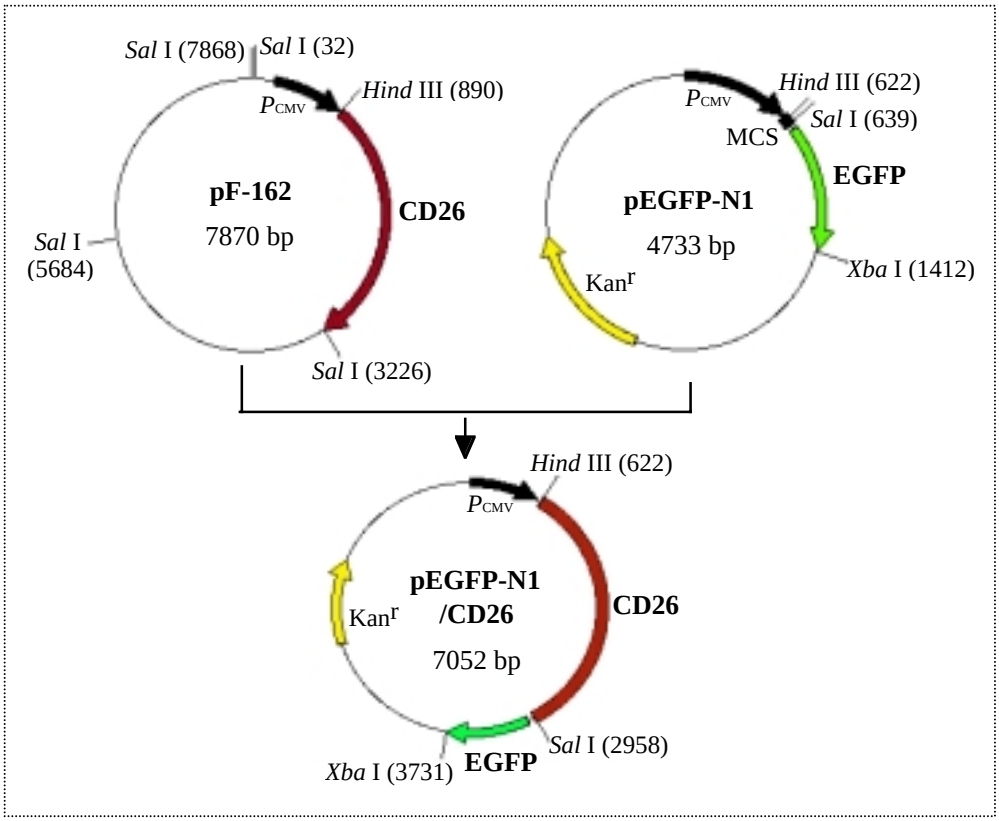

Fig 32. Schematic diagram of the construction of recombinant plasmid pEGFP-N1/CD26. pF-162 was digested by *Hind* III and *Sal* I to produce the fragment containing CD26 gene. This fragment was subsequently inserted into corresponding position in multiple cloning sites (MCS) of pEGFP-N1.

4.3.1.1 Construction of pEGFP-N1/CD26 recombinant plasmid

To construct pEGFP-N1/CD26 recombinant plasmid, pF-162 was first treated with *Sal* I and resulted in several fragments with different lengths. 34 bp (not visible), 2184 bp, 2458 bp and 3194 bp were produced by total digestion and other fragments due to incomplete digestion (Fig. 33A, Lane 2). The fragment of 3194 bp was isolated and extracted from preparative gel after electrophoresis separation. Further digestion of this fragment with

Hind III resulted in two fragments, 858 bp and 2336 bp (Fig. 33B, Lane 2). The fragment of 2336 bp containing cDNA of CD26 was isolated as insert for ligation.

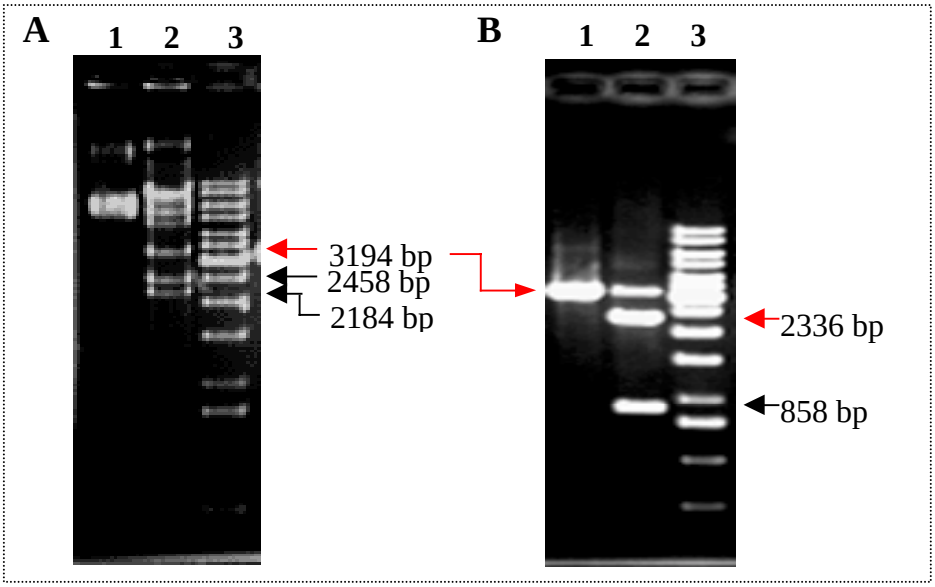

Fig. 33. Preparation and separation of DNA fragment containing complete rat CD26 gene from plasmid pF-162. A. Agarose gel electrophoresis of *Sal* I-digested pF-162. Lane 1: Intact pF-162, Lane 2: *Sal* I-digested pF-162, Lane 3: Marker. **B.** Agarose gel electrophoresis of *Hind* III-digested product of 3194 bp fragment. Lane 1: Fragment of 3194 bp isolated from *Sal* I-digested of pF-162, Lane 2: *Hind* III-digested product of 3194 bp fragment. Fragment of 2336 bp containing the cDNA of CD26 is indicated by red arrow. Lane 3: Marker.

The pEGFP-N1 vector was digested with the same enzyme combination, *Hind* III and *Sal* I. A band of 4716 bp was recovered from the gel. To prevent the recircularization of pEGFP-N1, the 5' phosphate ends of the linearized vector was removed by bacterial alkaline phosphatase (BAP) (Fig. 34A, lane 2).

The vector and insert DNA (Fig. 34B) were ligated and transformed into competent *E. coli* SCS 110 strain. The clones carrying correct recombinant plasmid were selected on LB Agar-plates by kanamycin resistance. SCS 110 is dam$^-$ *E.coli*. The plasmid expressed in this strain carries demethylated *Xba* I site, which is suitable for further cloning of CD26/GFP gene into response plasmid of Tet-on system.

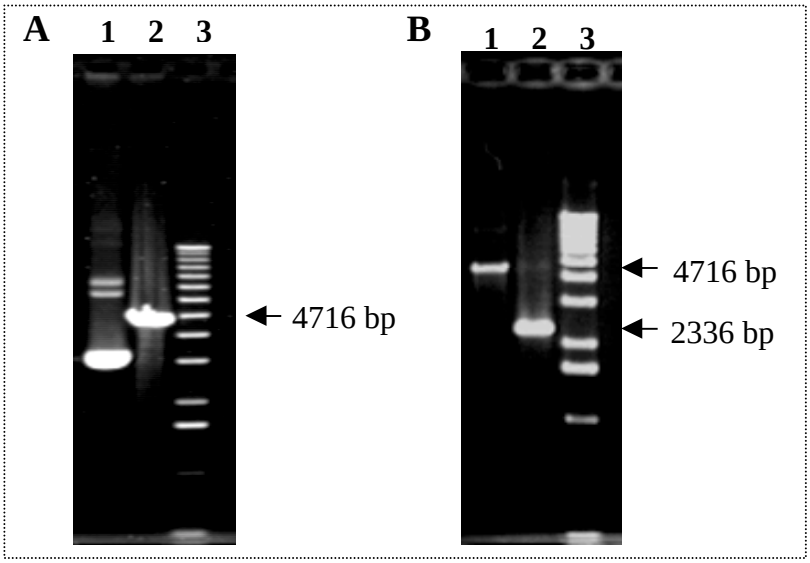

Fig. 34. Preparation of pEGFP-N1 vector DNA and ligation of vector and insert DNA. **A.** Agarose gel electrophoresis of pEGFP-N1 digested by combination of *Sal* I and *Hind* III. Lane 1: Intact pEGFP-N1, Lane 2: pEGFP-N1 digested by *Sal* I and *Hind* III, Lane 3: Marker. **B.** Agarose gel electrophoresis of isolated vector and insert DNA for ligation. Lane 1: *Sal* I and *Hind* III-digested pEGFP-N1 vector DNA; Lane 2: Insert DNA containing complete CD26 gene; Lane 3: Marker.

4.3.1.2 Screening of clones containing correctly recombinant plasmid

Twelve kanamycin resistant clones were selected. Plasmids, purified from the cultures of these clones by using mini QIAGEN plasmid purification kit, were digested into linear with *Hind* III and separated by gel electrophoresis. As shown in Fig. 35A, in comparison with molecular weight markers, among 12 clones, the size of plasmids from 11 clones is equal to calculated molecular weight (7052 bp) of recombinant plasmid carrying the cDNA encoding GFP as well as rat CD26. However clone 11 obviously contained only vector pEGFP-N1. For further determination, *Bgl* II was applied to digest plasmid of clone 1, 2, 3, 4, 5, 8, 9, 11 and 12 (Fig. 35B). The correctly recombinant plasmid should be cut into three fragments, 329 bp, 1875 bp and 4848 bp. While, due to unique digestion site of *Bgl* II, vector pEGFP-N1 should be cut into one fragment with molecular weight of 4733 bp. Results shown in Fig. 35B confirms that except clone 11, which contained only vector DNA, other clones contained correctly recombinant plasmid.

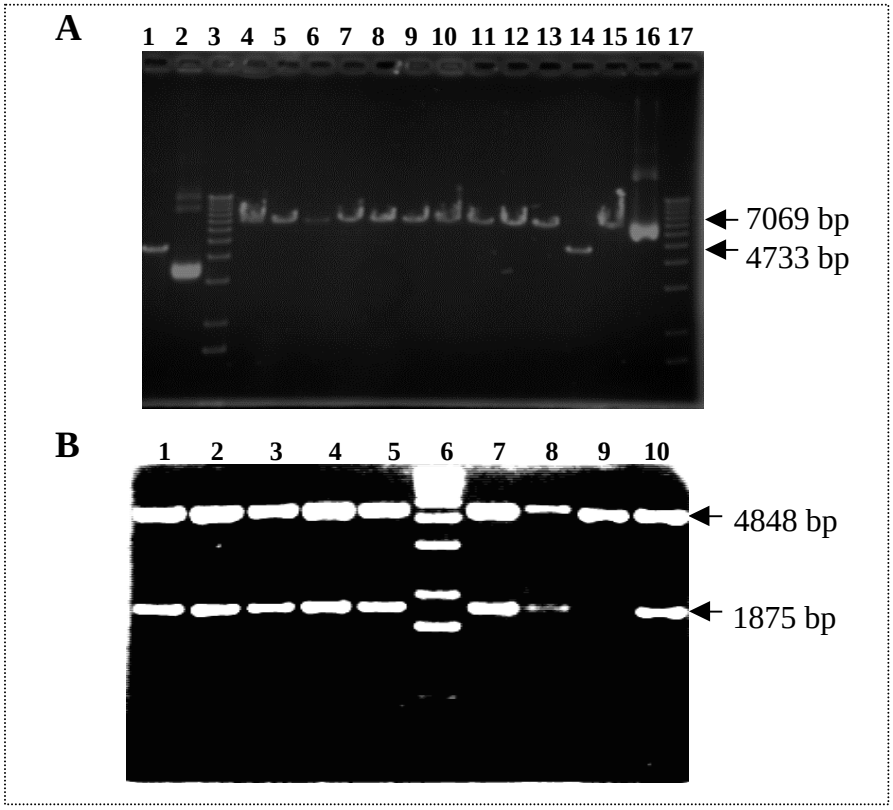

Fig. 35. Analysis of recombinant plasmid pEGFP-N1/CD26. **A.** Agarose gel electrophoresis of *Hind* III-digested pEGFP-N1/CD26. Lane 1: *Hind* III-digested pEGFP-N1, Lane 2: Intact pEGFP-N1, Lane 3: Marker, Lane 4-15: *Hind* III-digested plasmids purified from transformed clones 1-12. Lane 16: intact plasmid purified from clone 1. Lane 17: Marker. **B.** Agarose gel eletrophoresis of *Bgl* II-digested pEGFP-N1/CD26. Lane 1-5, 7-10, *Bgl* II-digested plasmid purified from transformed clones 1-5, 8, 9, 11, 12. Lane 6: Marker.

4.3.1.3 Expression of CD26/GFP fusion protein in CHO cells

Recombinant plasmids were transfected into CHO cells. The expression of the fusion protein CD26/GFP in CHO transfectants was determined by fluorescence microscopy (Fig. 36), FACScan cytometry (Fig. 37) and DPPIV enzyme activity (Fig. 38). Fig. 36 and 37A showed that fusion protein retained the fluorescent properties of GFP. CD26 in fusion protein was recognized by its mAb (Fig. 37B) and exhibited DPPIV enzyme activity (Fig. 38).

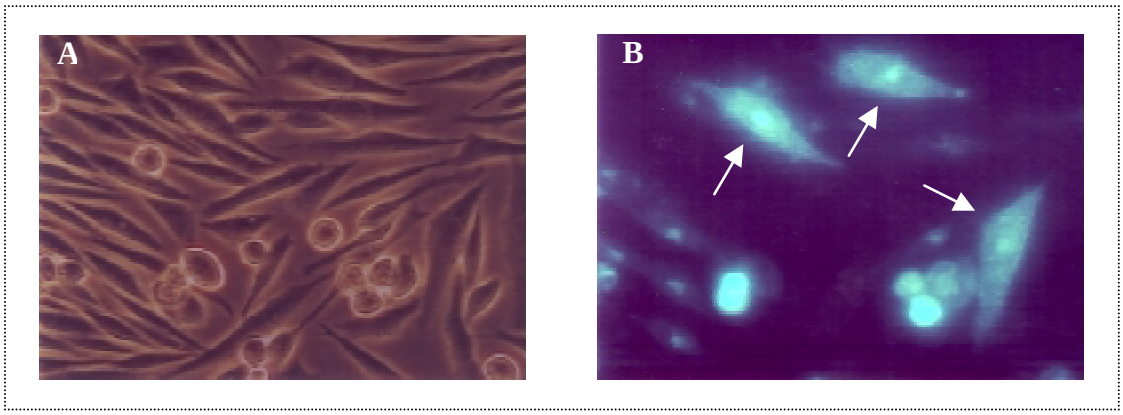

Fig. 36. Micrograph of fusion protein CD26/GFP expression in CHO transfectants. A and **B** are the same microfield. **A**. Phase-contract image. **B.** Fluorescence image. Cells expressing GFP were indicated by arrows.

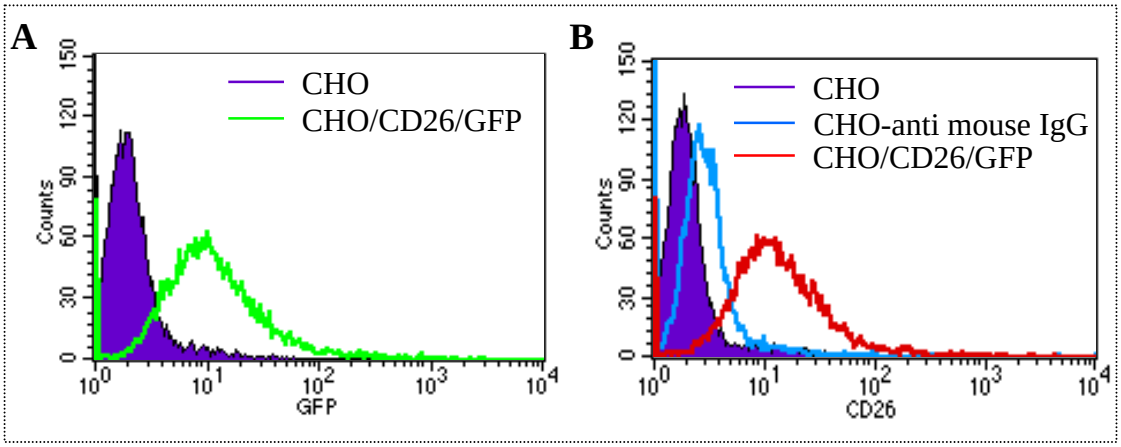

Fig. 37. FACS analysis of fusion protein CD26/GFP expression in CHO transfectants. A. GFP expression. **B.** CD26/DPPIV expression. Anti-rat CD26 mAb was used for immunostaining. Cells were analyzed by flow cytometry.

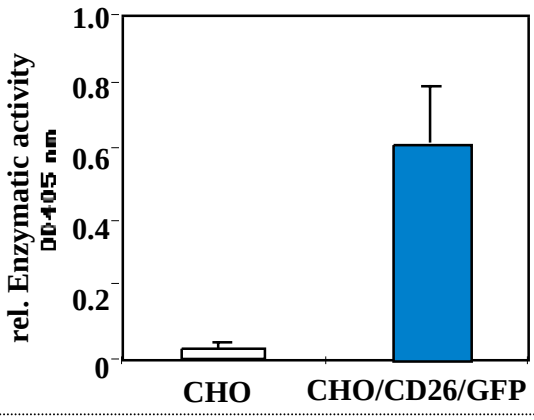

Fig. 38. DPPIV activity of fusion protein CD26/GFP. CHO transfectants were solubilized and DPPIV enzyme activity was measured as described in material and methods. The noted valueds represent the mean ± SD of three experiments.

4.3.2 Construction of a recombinant plasmid pTRE2/CD26/GFP

4.3.2.1 Cloning of CD26/GFP cDNA into response plasmid pTRE2

Cloning of CD26/GFP cDNA into response plasmid pTRE2 of Tet-on system was shown in Fig. 39. Both plasmid pEGFP-N1/CD26 and pTRE2 were treated with *Xba* I and *Hind* III. The fragment containing CD26/GFP gene from pEGFP-N1/CD26 was then inserted into corresponding position in multiple cloning sites (MCS) immediately downstream of Tet-responsive promoter of pTRE2. The transcription of CD26/GFP gene will be controlled by tetracycline-response element (TRE).

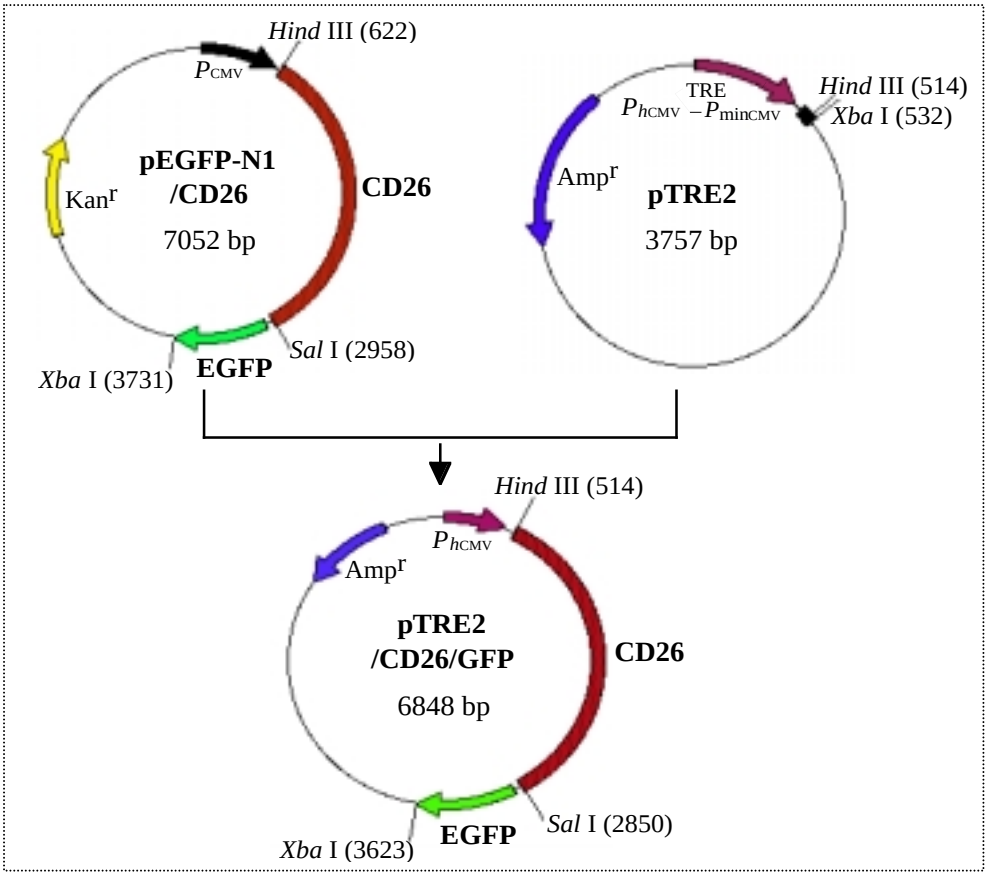

Fig. 39. Schematic diagram of the cloning of CD26/GFP cDNA into response plasmid pTRE2. pEGFP-N1/CD26 was digested by *Xba* I and *Hind* III to produce the fragment encoding CD26 and GFP. This fragment was cloned in corresponding position in MCS of pTRE2 immediately downstream of Tet-on responsive promoter.

After treatment with *Xba* I, the plasmid pGFP-N1/CD26 was cut into linear DNA as shown in Fig. 40A, Lane 2. This linear DNA was extracted from preparative gel after electrophoretic separation. Then it was further digested by *Hind* III into two fragments of 3109 bp and 3960 bp (Fig. 40A, Lane 3). The fragment of 3109 bp containing cDNA of CD26/GFP was isolated as insert for ligation.

The vector pTRE2 was digested with *Xba* I and then with *Hind* III (Fig. 40A, Lane 6 and 7). A band of 3739 bp was recovered from the gel. To prevent the recircularization of pTRE2, the 5' phosphate ends of the linearized vector was removed by BAP.

The isolated vector and insert DNA (Fig. 40B) were ligated. This ligation was transformed into *E. coli* HB 101. The clones harboring recombinant plasmid were selected on LB plates by Ampicillin resistance.

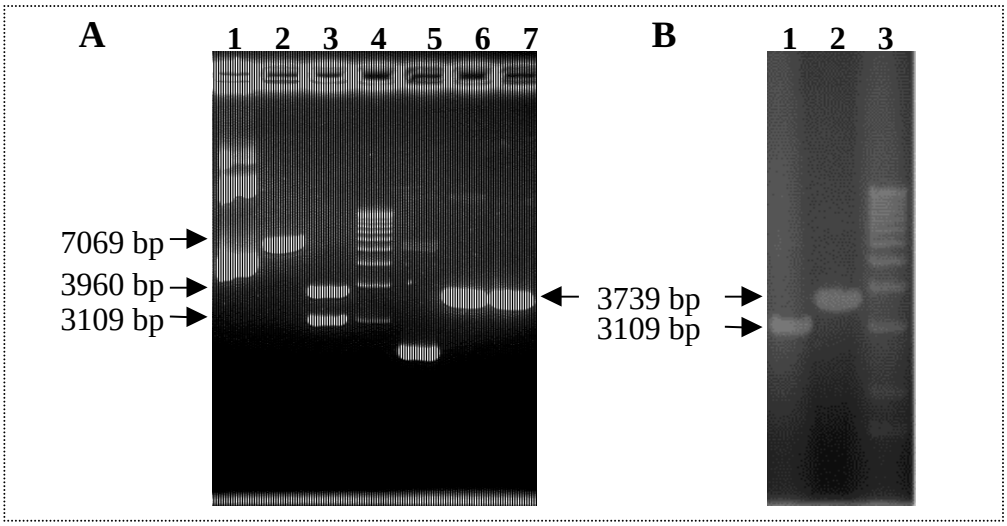

Fig. 40. Preparation of insert and vector DNA for construction of recombinant plasmid pTRE2/CD26/GFP. A. Preparation of insert and vector DNA. Lane 1: Intact pGFP-N1/CD26, Lane 2: *Xba* I-digested pGFP-N1/CD26, Lane 3: pGFP-N1/CD26 digested by combination of *Xba* I and *Hind* III, Lane 4: Marker, Lane 5: Intact pTRE2, Lane 6: *Xba* I-digested pTRE2, Lane 7: *Xba* I and *Hind* III-digested pTRE2. **B.** Agarose gel electrophoresis of vector and insert DNA for ligation. Lane 1: Insert DNA, Lane 2: Vector DNA, Lane 3: Marker.

4.3.2.2 Screening of clones containing recombinant plasmid pTRE2/CD26/GFP

Four ampicillin resistant clones were selected. Plasmids, purified from the cultures of these clones by using mini QIAGEN plasmid purification kit, were digested with *Hind* III into linear and separated by gel electrophoresis. As shown in Fig. 41A, in comparison with molecular weight of markers, the size of plasmids from 3 of 4 clones was 6848 bp, which corresponds to the calculated molecular weight of recombinant plasmid (Fig. 41A, Lane 2-4). Whereas, clone 4 obviously contained only vector pTRE2 (Fig. 41A, Lane 5). For further confirmation, *Sal* I was applied following *Hind* III treatment to digest plasmid from clone 2. The recombinant plasmid was cut into two fragments, 2336 bp, 4512 bp (Fig. 41B, Lane 1), which was consistent with calculated correct construction. Fig. 41B, Lane 2 showed there was three fragments after *Bgl* II digestion with molecular weight 1641 bp, 1875 bp and 3332 bp, respectively, confirming clone 2 contained the correct recombinant plasmid.

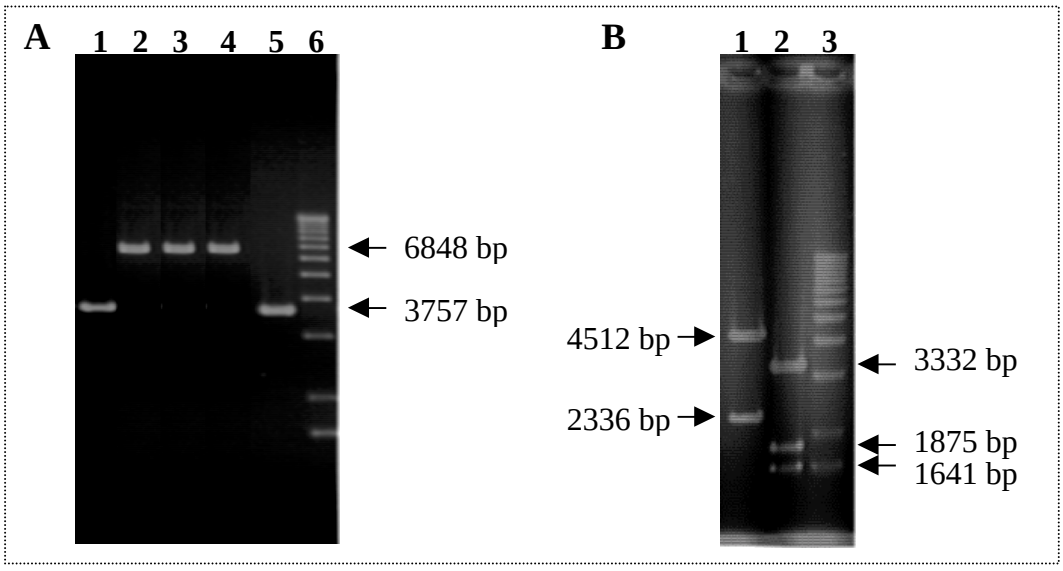

Fig. 41. Examination of recombinant plasmid pTRE2/CD26/GFP. A. Agarose gel electrophoresis of *Hind* III-digested pTRE2/CD26/GFP. Lane 1: *Hind* III-digested pTRE2, Lane 2-5: *Hind* III-digested plasmids purified from clones 1-4. Lane 6: Marker. **B.** Agarose gel electrophoresis of *Hind* III/*Sal* I- or *Bgl* II-digested plasmid purified from clone 2. Lane 1: *Hind* III/*Sal* I-digested recombinant plasmid, Lane 2: *Bgl* II digested-recombinant plasmid, Lane 3: Marker.

4.3.3 Establishment of inducible expression system of CD26 in Jukat cells

Construction of inducible expression system of CD26 gene in Jukat cells was shown in Fig. 42. At first, plasmid pTet-On was transfected into Jurkat cells. Clones transfected with pTet-on were selected by G418. Subsequently pTER2/CD26/GFP and pTK-Hyg were co-transfected into 30 of G418-resistant clones and double-transfectants were selected in presence of hygromycin and G418.

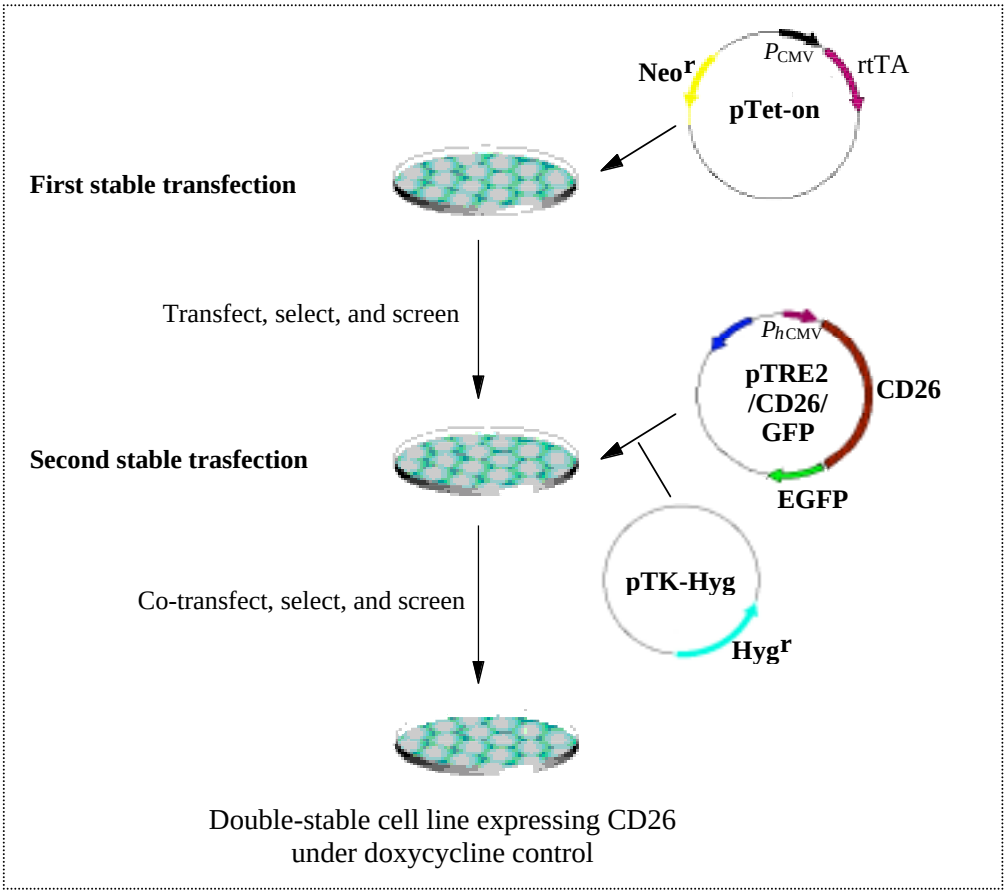

Fig. 42. Schematic diagram of the establishment of Tet on expression system of CD26/GFP fusion protein in Jurkat cells.

The expression of CD26 in these transfectants was induced by over night incubation with 2 µg/ml doxycycline. Fig. 43 showed the doxycycline induced expression of fusion protein CD26/GFP on Jurkat cells. Without doxycycline, no expression of CD26/GFP fusion

protein was observable (Fig. 43E and F). Following doxycycline addition, a high expression of this protein was visualized by fluorescence microscopy (Fig. 43B and D).

Therefore, the inducible expression system of CD26/GFP fusion protein in Jurkat cells was well established. The function of CD26 expression in Jurkat cells is on going in our laboratory.

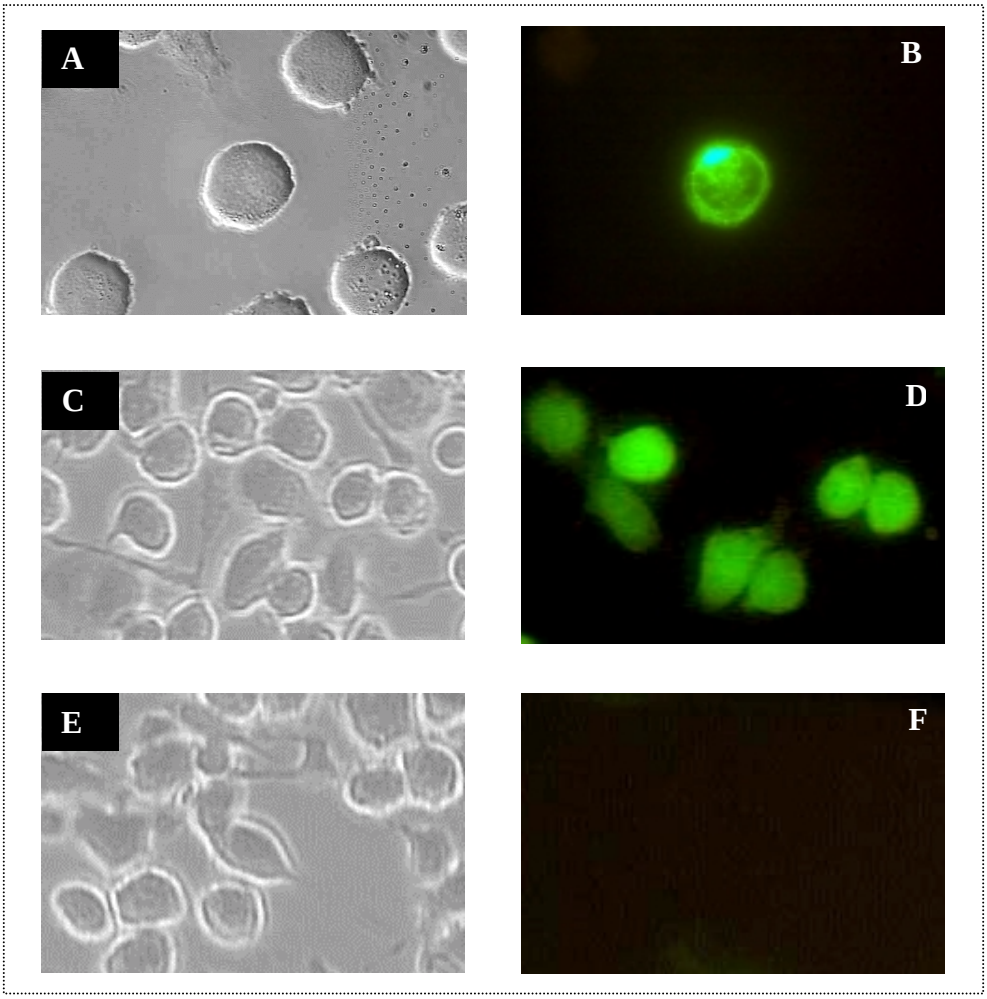

Fig. 43. Micrograph of inducible expression of fusion protein CD26/GFP in Jurkat cells. A & **B, C** & **D** and **E** & **F** are the same microfield respectively. **A, C** and **E,** phase contract image. **B, D** and **F,** Fluorescence image. **A** & **B**, doxycycline (2 µg/ml) induced expression of fusion protein CD26/GFP in Jurkat cells in suspension. **C** & **D**, doxycycline (2 µg/ml) induced expression of fusion protein CD26/GFP in fibronectin-immobilized Jurkat cells. **E** & **F**, tranfectants on fibronectin coated plates without doxycycline.